To appear in ApJ
Preprint typeset using LaTeX style emulateapj v. 11/12/01

IMPROVED MEASUREMENTS OF THE CMB POWER SPECTRUM WITH ACBAR

C.L. Kuo[1,2], P.A.R. Ade[3], J.J. Bock[1,2], J.R. Bond[4], C.R. Contaldi[4,5], M.D. Daub [6], J.H. Goldstein[7], W.L. Holzapfel [6], A.E. Lange[1,2], M. Lueker[6], M. Newcomb[8], J.B. Peterson[9], C. Reichardt[1], J. Ruhl[7], M.C. Runyan[10], Z. Staniszweski[7]

To appear in ApJ

ABSTRACT

We report improved measurements of temperature anisotropies in the cosmic microwave background (CMB) radiation made with the Arcminute Cosmology Bolometer Array Receiver (ACBAR). In this paper, we use a new analysis technique and include 30% more data from the 2001 and 2002 observing seasons than the first release (Kuo et al. 2004) to derive a new set of band-power measurements with significantly smaller uncertainties. The planet-based calibration used previously has been replaced by comparing the flux of RCW38 as measured by ACBAR and BOOMERANG to transfer the WMAP-based BOOMERANG calibration to ACBAR. The resulting power spectrum is consistent with the theoretical predictions for a spatially flat, dark energy dominated ΛCDM cosmology including the effects of gravitational lensing. Despite the exponential damping on small angular scales, the primary CMB fluctuations are detected with a signal-to-noise ratio of greater than 4 up to multipoles of $\ell = 2000$. This increase in the precision of the fine-scale CMB power spectrum leads to only a modest decrease in the uncertainties on the parameters of the standard cosmological model. At high angular resolution, secondary anisotropies are predicted to be a significant contribution to the measured anisotropy. A joint analysis of the ACBAR results at 150 GHz and the CBI results at 30 GHz in the multipole range $2000 < \ell < 3000$ shows that the power, reported by CBI in excess of the predicted primary anisotropy, has a frequency spectrum consistent with the thermal Sunyaev-Zel'dovich effect and inconsistent with primary CMB. The results reported here are derived from a subset of the total ACBAR data set; the final ACBAR power spectrum at 150 GHz will include 3.7 times more effective integration time and 6.5 times more sky coverage than is used here.

Subject headings: cosmic microwave background — cosmology: observations

1. INTRODUCTION

Observations of the cosmic microwave background (CMB) radiation on angular scales corresponding to multipole values of $\ell \lesssim 1000$ have established a "concordance" cosmological model characterized by a negligible spatial curvature, 5% baryonic matter, 25% dark matter, and 70% dark energy (Spergel et al. 2006), in good agreement with results from other cosmic probes (Tegmark et al. 2004; Riess et al. 2004; Burles et al. 2001). On smaller angular scales, the CMB anisotropy is exponentially damped by photon diffusion. The damping scale is a measure of the angular size of the Silk length at the surface of last scattering (Silk 1968; Bond & Efstathiou 1984; Hu & White 1997). This portion of the CMB power spectrum, known as the "damping tail", provides a consistency check of the cosmological model and independent constraints on several cosmological parameters.

At 150 GHz, anisotropies from the thermal Sunyaev-Zel'dovich (SZ) effect are expected to dominate over the primary CMB fluctuations for multipoles $\ell > 2500$. The fluctuation power of this "SZ excess" depends sensitively on the integrated cluster abundance and cluster gas distribution. Accurate measurements of the SZ fluctuation amplitude provide an independent measurement of the amplitude of matter perturbations, usually characterized by σ_8.

The Arcminute Cosmology Bolometer Array Receiver (ACBAR) is designed to study both primary and secondary CMB anisotropies on small angular scales (Runyan et al. 2003). The fundamental features of the angular power spectrum in the range $\ell \lesssim 1000$ have been characterized by several ground, balloon, and satellite-based experiments. The damping of CMB anisotropy power at $\ell \gtrsim 1000$ has been measured by the Cosmic Background Imager (CBI) (Pearson et al. 2003; Readhead et al. 2004a), ACBAR, and the Very Small Array (VSA) (Dickinson et al. 2004). The excellent agreement between the observed CMB damping tail power spectrum and the theoretical predictions of the ΛCDM model provide compelling evidence that our interpretation of the

[1] Observational Cosmology, California Institute of Technology, MS 59-33, Pasadena, CA 91125
[2] Jet Propulsion Laboratory, 4800 Oak Grove Drive, Pasadena, CA 91109
[3] Department of Physics and Astronomy, Cardiff University, CF24 3YB Wales, UK
[4] Canadian Institute of Theoretical Astrophysics, University of Toronto, Toronto, Ontario, M5S3H8, Canada
[5] Blackett Laboratory, Imperial College, Prince Consort Road, London, SW7 2AZ, U.K.
[6] Department of Physics, University of California, Berkeley, CA 94720
[7] Department of Physics, Case Western Reserve University, Cleveland, OH 44106
[8] Yerkes Observatory, 373 W. Geneva Street, Williams Bay, WI 53191
[9] Department of Physics, Carnegie Mellon University, Pittsburgh, PA 15213
[10] Department of Physics, University of Chicago, Chicago IL 60637

CMB is correct.

The high resolution CMB anisotropy measurements reported here extend the low-ℓ results, such as those from the WMAP satellite, to a comoving scale of $\sim$ 5 Mpc, and provide strong constraints on the shape of the primordial density perturbation spectrum (Peiris et al. 2003; Mukherjee & Wang 2003; Bridle et al. 2003; Leach & Liddle 2003). The primordial spectrum is close to scale-invariant, consistent with predictions of slow-roll inflation models. Departures from scale-invariance provide valuable clues to the physics of the early Universe.

Measurements of the high-ℓ CMB anisotropy power at 30 GHz by CBI (Mason et al. 2003; Bond et al. 2005) and BIMA (Dawson et al. 2006) detect power in excess of the predictions of the standard cosmological model. If interpreted as the thermal SZ effect produced by clusters of galaxies, this excess power corresponds to a value of σ_8 that is slightly higher than the value found by analysis of optical galaxy clustering (Tegmark et al. 2004; Efstathiou et al. 2002). This result hinges upon the excess fluctuation power seen by the CBI, which could be the result of contamination by a population of low-flux flat-spectrum radio sources. This possibility is being investigated with a 30 GHz continuum receiver at the Green Bank Telescope (Mason et al. 2005). Alternative origins of the excess involve non-standard ingredients in the cosmological model, such as, primordial voids and magnetic fields (Griffiths et al. 2003; Subramanian et al. 2003). The frequency spectrum of the thermal SZ effect is distinctly different from that of the primordial anisotropy. ACBAR observes at a much higher frequency than BIMA or the CBI (150 GHz versus 30 GHz), and the addition of the ACBAR high-ℓ measurements can be used to constrain the possible origin of any observed excess.

The first ACBAR power spectrum, presented by Kuo et al. (2004) (K04), was produced from the Lead-Main-Trail (LMT) analysis of a subset of the first two years of ACBAR observations. Three major improvements are made in this work over that first release. First and most importantly, the power spectrum is derived from the un-differenced temperature maps (rather than "Lead-Main-Trail" subtracted maps), significantly reducing the uncertainties from cosmic variance and instrumental noise. Second, we replace the planet-based calibration with a more precise calibration based on the flux of RCW38 as measured by ACBAR and BOOMERANG (Crill et al. 2003). Third, we include two additional CMB fields observed late in the 2002 season which were not used in previous publications. These fields increase the total data volume by $\sim 30\%$.

This paper is organized as follows. In § 2 we review the ACBAR instrument and the CMB observation program. The new analysis algorithm for the un-differenced maps is explained in § 3. Section § 4 is an overview of the calibration using RCW38; the details of cross-calibration between BOOMERANG and ACBAR are discussed in Appendix A. Systematic tests and foreground contamination are discussed in § 5. We present the band-power results in § 6, including a discussion of the scientific interpretation. The ACBAR band powers are combined with the results of other experiments to place constraints on the parameters of cosmological models in § 7. The main results of this paper are summarized in § 8.

2. THE INSTRUMENT AND OBSERVATIONS

The ACBAR instrument was designed to be used with the Viper telescope at the South Pole to observe CMB temperature anisotropies with an angular resolution of $5'$. The receiver consists of 16 bolometers, coupled to the 2-meter off-axis Gregorian telescope through corrugated feed horns. The bolometers are cooled to 240 mK by a 3-stage He^3-He^3-He^4 sorption refrigerator. The beams from the array are swept across the sky at near-constant elevation by the motion of a flat tertiary mirror. The receiver was deployed in December 2000, and CMB data were taken during the austral winters of 2001, 2002, 2004, and 2005. The bolometer array was reconfigured between the 2001 and 2002 observing seasons to double the number of 150 GHz detectors; details of the instrument configuration and performance in each season are given in Runyan et al. (2003), while details of the CMB observations, data reduction procedures, and beam maps can be found in K04.

The results reported here are derived from the 150 GHz data gathered in the 2001 and 2002 Austral winters. These data come from observations of four independent CMB fields, detailed in Table 1. The power spectrum derived from the first two fields, CMB2/CMB4 and CMB5, was reported in K04. Since then, we have completed the analysis of two additional fields, CMB6 and CMB7, observed in July and August of 2002. Each of these four widely-separated fields was chosen to include a bright quasar, the image of which provides an important check of the telescope pointing over the entire observation period.

We derive the noise properties of the data from the raw time streams. The photon noise and bolometer noise are white, Gaussian distributed, and uncorrelated between bolometers. On the other hand, "sky noise" associated with atmospheric fluctuations can introduce correlations between bolometers. This noise component can be described by the Kolmogorov-Taylor theory, which models the turbulence as a screen of frozen fluctuations blown through the field of view with a certain wind speed. The sky noise properties of the South Pole characterized with ACBAR are reported in detail by Bussmann et al. (2005). In the CMB power spectrum analysis, we calculate the full cross-channel correlations and use them as a data cut. We disregard data that show cross-channel correlations (after removal of up to a 10th order polynomial from each chopper sweep) higher than 5% of the total noise power.

3. UN-DIFFERENCED POWER SPECTRUM ANALYSIS

Following the conventions of the first data release, the band-powers $\mathbf{q}$ are reported in units of μK^2, and are used to parameterize the power spectrum according to

$$\ell(\ell+1)C_\ell/2\pi \equiv \mathcal{D}_\ell = \sum_B q_B \chi_{B\ell} \,, \qquad (1)$$

where $\chi_{B\ell}$ are tophat functions; $\chi_{B\ell} = 1$ for $\ell \in B$, and $\chi_{B\ell} = 0$ for $\ell \notin B$. The observations in 2001 and 2002 were carried out in a *lead-main-trail* (LMT) pattern in order to facilitate the removal of slowly varying time-dependent chopper synchronous offsets. In the analysis of

TABLE 1
CMB FIELDS

Field	RA (deg)	dec (deg)	Area (deg^2)	Time (hrs.)	Year	# of detectors
CMB2(CMB4)	73.963	-46.268	44(28)	506(142)	2001(2002)	4(8)
CMB5	43.372	-54.698	31	1656	2002	8
CMB6	32.693	-50.983	29	351	2002	8
CMB7	338.805	-48.600	32	420	2002	8

Note. — The central quasar coordinates and size of each CMB field observed by ACBAR during 2001 and 2002. The fifth column gives the detector integration time for each field after cuts. This represents approximately 50% of the total time spent observing CMB fields. The last column gives the number of 150 GHz detectors.

K04, we differenced the CMB maps according to the formula $M-(L+T)/2$, and derived the band-powers from the differenced maps. While this conservative strategy can prevent potential systematic errors, it increases the effect of instrumental noise and reduces sky information. At high-ℓ, where the uncertainties in the band-powers are dominated by the instrument noise, the anisotropy power signal-to-noise ratio (S/N) derived from a LMT differenced map is a factor of

$$\eta_{LMT}=\frac{SN_{LMT}}{SN_0}=$$

$$\left[\frac{\sqrt{1^2+(1/2)^2+(1/2)^2}}{\sqrt{\sqrt{2}^2+(\sqrt{4}/2)^2+(\sqrt{4}/2)^2}}\right]^2=\frac{3}{8}$$

smaller than that for an un-differenced map with an identical amount of observing time (ignoring the small correlations between differenced fields). The higher noise in L and T reflects the reduced (50%) observing time on these fields compared to the main field.

It is possible to generalize the noise-weighted co-added map analysis outlined in K04 to avoid this S/N degradation, while ensuring that the power spectrum is not contaminated by the chopper synchronous signals. The key to this generalization lies in the fact that the band-powers can be derived from arbitrary linear combinations of the time stream. The linear combinations can be constructed such that the un-differenced maps are cleaned of chopper synchronous offsets. The results presented in § 6 are derived from such "cleaned", un-differenced maps, using the method outlined below.

Suppose d_α ($\alpha=1..n_t$) are n_t time-ordered measurements of CMB temperature. This vector is the sum of the noise component n_α and the signal component s_α. The data from each chopper sweep are filtered to remove chopper synchronous offsets before they are co-added. For example, since the beams approximately follow a great circle on the celestial sphere, changing the chopper angle causes the detectors to look through a different atmosphere thickness and produces signals that are functions of the chopper position. Formally, the filtering is done by operating on the time stream $\mathbf{d}$ with the "corrupted mode projection" matrix $\mathbf{\Pi}$. This operation results in the cleaned time stream $\tilde{\mathbf{d}}\equiv\mathbf{\Pi d}$.

Large angular scale chopper offsets are largely removed by this mode projection. In the analysis of K04, any residual small angular scale offsets were eliminated through LMT differencing. Alternatively, chopper synchronous offsets can be removed by subtracting the average chopper function, determined with the whole map, from the individual data strips (Runyan 2002). However, this assumes that the offsets do not change in time and elevation. In this paper, we remove a chopper synchronous offset from each data strip where the amplitude of the offset at each sample in the strip is free to vary quadratically with elevation in the map. The mean of these quadratic functions in elevation gives the mean chopper function; at zeroth order, the mean chopper function is removed. The quadratic variation allows for slow changes in the synchronous offset as a function of time and elevation. Projecting out these corrupted modes eliminates any detectable residual chopper offset with minimal loss of signal in the final power spectrum. The loss of information at high-ℓ is negligible, since the data contain many more degrees of freedom than the removed modes do.

Mathematically, the corrupted mode projection matrix Π is now the product of two matrices, $\Pi\equiv\Pi_2\Pi_1$. The operator Π_1 is the original Π matrix used by K04 that adaptively removes polynomial modes in RA, where the order of the polynomial removed typically depends on the atmospheric conditions. The additional operator Π_2 removes quadratic modes in DEC independently for each of the lead, main, and trail fields. We perform systematic tests in §5 to confirm that any residual offset is smaller than the noise level of the final power spectrum. The resulting time stream $\tilde{\mathbf{d}}$ is then co-added into a map $\mathbf{T}$ according to the telescope pointing model. Next, a signal-to-noise eigenmode truncation is applied, and only the modes expected to have non-negligible signal-to-noise ratio are retained. This significantly reduces the computational requirements of the analysis. Since both the projection of corrupted modes and signal-to-noise eigenmode truncation are linear operations, the resulting data vector $\mathbf{\Delta}$ is also a linear combination of the original time stream, represented by

$$\mathbf{\Delta}=\mathbf{Ld}.$$

The noise covariance matrix is given by

$$\mathbf{C}_N=\mathbf{L}\langle\mathbf{nn}^t\rangle\mathbf{L}^t.$$

The signal component in the time stream $\mathbf{s}$ is the convolution of sky map $\mathfrak{T}(\mathbf{r})$ with $B_\alpha(\mathbf{r})$, the beam function

during measurement α,

$$s_\alpha = \int d^2r \mathfrak{T}(\mathbf{r}) B_\alpha(\mathbf{r}).$$

The signal component of Δ is

$$\Delta_i^{sig} = \sum_\alpha L_{i\alpha} s_\alpha \equiv \int d^2r F_i(\mathbf{r}) \mathfrak{T}(\mathbf{r}), \quad (2)$$

where the pixel-beam function F_i is given by

$$F_i(\mathbf{r}) = \sum_\alpha L_{i\alpha} B_\alpha(\mathbf{r}). \quad (3)$$

In the flat sky limit, the theory covariance matrix is given by

$$C_{T\{ij\}} = \langle \Delta_i \Delta_j \rangle^{sig} = \int\int d^2r d^2r' F_i(\mathbf{r}) F_j(\mathbf{r}') \langle \mathfrak{T}(\mathbf{r}) \mathfrak{T}(\mathbf{r}') \rangle$$
$$= \int\int d^2r d^2r' F_i(\mathbf{r}) F_j(\mathbf{r}') \int \frac{d^2l}{(2\pi)^2} C_\ell \cdot e^{i\mathbf{l}\cdot(\mathbf{r}-\mathbf{r}')}$$
$$= \int \frac{d^2\ell}{(2\pi)^2} C_\ell \cdot \tilde{F}_i^*(\mathbf{l}) \tilde{F}_j(\mathbf{l}), \quad (4)$$

where $\tilde{F}_i(\mathbf{l})$ is the Fourier transform of $F_i(\mathbf{r})$. To perform the iterative quadratic band-power estimation procedure, it is necessary to know the partial derivative of C_T with respect to each of the band-powers q_B, which according to equation(1) is given by

$$\frac{\partial C_{T\{ij\}}}{\partial q_B} = \int \frac{d^2\ell}{(2\pi)^2} \frac{2\pi\chi_{B\ell}}{\ell(\ell+1)} \cdot \tilde{F}_i^*(\mathbf{l}) \tilde{F}_j(\mathbf{l}). \quad (5)$$

Note that this algorithm does not assume that the instrument beams stay constant during the observations. As described in Runyan et al. (2003), the ACBAR beam sizes are weak functions of the chopper position. K04 adopted a semi-analytic expansion to correct for these effects to first order. To verify that the effects due to non-uniform beams are small, we developed two end-to-end pipelines. In the first pipeline, the pixel-beam functions $F_i(\mathbf{r})$ are calculated explicitly during the co-adding process. The bandpowers in Table 3 are analyzed with this algorithm. In the second pipeline, an averaged beam is used for the entire map. The difference in the power spectra from the two pipelines is negligible.

In the analysis of K04, we assumed that the noise is stationary in chopper position after LMT subtraction. In the current treatment, we relax this assumption and calculate the full two dimensional correlation matrix directly from the time stream data without using Fourier transforms.

All the numerical calculations are performed on the National Energy Research Scientific Computing Center (NERSC) IBM SP RS/6000. The evaluation of $\tilde{F}_i(\mathbf{r})$ and its Fourier transform are the most computationally demanding steps in this analysis. After $\mathbf{C}_T$, $\mathbf{C}_N$ and $\mathbf{C}_{T,B}$ are calculated, standard likelihood maximizing procedures are used to find the band-powers $\mathbf{q}_B$ and uncertainties (Bond et al. 1998). The results of this analysis are presented in Table 3 and Figure 1.

4. CALIBRATION

RCW38 is a compact HII region in the Galactic plane at a declination similar to the ACBAR CMB fields. It has a large and stable flux and serves as the primary calibrator for the ACBAR observations. We determine the absolute flux of RCW38 using maps from the 2003 flight of BOOMERANG (Masi et al. (2006), hereafter B03), which are calibrated relative to the WMAP experiment with an absolute uncertainty of 1.8%. RCW38 does not have a black-body spectrum, requiring spectral corrections for the calibration of CMB anisotropies. However the similarity in the spectral responses of the 150 GHz bands in the B03 and ACBAR experiments ensures these corrections to be small. Here we outline the calibration procedure, leaving the details to Appendix A.

ACBAR typically observed RCW38 before and after each CMB observation. Comparisons between the B03 and ACBAR maps of RCW38 are used to determine the absolute calibration of the CMB fields to an uncertainty of 6.0%. For roughly 50% of the 2002 season, we observed RCW38 with only half the 150 GHz detectors (4 out of 8). During these periods, the RCW38 calibration was applied to the remaining detectors by comparing CMB power spectra derived from each half of the detectors. The calibration of the CMB4 field (observed in 2002) is extended to the 70% overlapping CMB2 field (observed in 2001) by comparing power spectra from each field. In the first ACBAR release, the 2001 and 2002 data sets were calibrated with an accuracy of 10% using observations of Mars and Venus respectively. We determine the corrections to this planet-based calibration to be 0.911±0.072 for CMB2 (2001) and 1.128±0.066 for CMB4-7 (2002) in CMB temperature. The 2002 observations dominate the final power spectra, and the final results have essentially the same 6% temperature calibration uncertainty as the 2002 data.

5. SYSTEMATIC UNCERTAINTIES AND FOREGROUNDS

5.1. *Jackknife Tests*

We performed a series of tests to constrain the amplitude of potential systematic errors in the power spectrum results. As described by K04, the "first half minus second half" jackknife is a very powerful test for time dependent errors, such as a changing calibration, inconsistency in the beam or pointing reconstruction, and time varying sidelobe pickup. In addition, high-ℓ jackknife band-powers constrain the mis-estimation of noise. We perform this test on the joint CMB power spectrum and find the bandpowers of the chronologically differenced maps are consistent with zero (Fig. 2).

Similarly, the data can be divided in two halves according to the direction of the chopper motion. Microphonic vibrations due to the chopper turn-arounds, erroneous transfer function corrections, or effects of wind direction could produce a nonvanishing signal in the jackknife band-powers. We find that the power spectrum of the left-right differenced maps is also consistent with zero.

To ensure that any residual chopper synchronous offset is below the noise level, we have developed a new systematic test that *enhances* the contribution of any such offsets relative to the CMB. In this test, the band-powers are derived from an LMT *sum* map, $L + M + T$, in which the residual synchronous offsets (the same in each field) are enhanced relative to the (random) CMB fluctuations by a factor of 3 in power (neglecting the small correlations at low-ℓ). The resulting band-powers are compared with the un-differenced band-powers to check for systematic deviations. This test is particularly sensitive to any resid-

ual chopper offsets. We find no significant deviation in the LMT sum band-powers from the un-differenced band-powers. When compared with the model ΛCDM power spectrum, we do notice a slight rise in the LMT sum band-powers for $\ell > 2300$. It is difficult to assess the significance or the origin of this low level trend. However, even if it is caused by a residual systematic effect, the contribution to the joint band-powers would be smaller than the statistical uncertainty in the reported band powers in this paper after accounting for the factor of 3 amplification.

5.2. *Foregrounds*

At frequencies below the peak of the CMB intensity (~ 200 GHz), the contribution of extra-galactic radio point sources to the observed CMB temperature anisotropy decreases rapidly with increasing observing frequency. In addition to the negative spectral indices of the majority of the radio sources, the flux-to-temperature conversion factor, $(dB_\nu/dT_{CMB})^{-1}$, reaches a minimum as the observing frequency approaches the peak of the CMB. In particular, this factor is nearly 15 times smaller at 150 GHz than at 30 GHz. The measurements of ACBAR are therefore much less susceptible to contamination by radio point sources than experiments operating at 30 GHz such as CBI, BIMA, and VSA. We construct templates using the positions of the known radio sources from the 4.85 GHz Parkes-MIT-NRAO (PMN) survey (Wright et al. 1994), and project out their contributions to the power spectrum estimations. Using the method described by K04, we remove them from the data without making assumptions about their fluxes. Of 200 PMN sources in the observed CMB fields, we detected the guiding quasars and six additional sources with significance greater than $> 2.8\sigma$. These sources tend to have shallow, and in some cases inverted spectral indices. Table 2 lists the parameters of the PMN sources that are detected in the ACBAR fields; the detection threshold of $> 2.8\sigma$, corresponds to a false detection rate of 1. The uncertainties are calculated using Monte-Carlo simulations, and are dominated by contributions from CMB primary anisotropies. With the exception of the guiding quasar in each of the CMB fields, the effect of removing the point sources on the band-powers is not significant.

Thermal emission from interstellar dust also has the potential to contaminate the measured power spectrum. The ACBAR CMB fields are located in the regions of low Galactic dust emission. Finkbeiner et al. (1999) (FSD) combined observations from IRAS, COBE/DIRBE, and COBE/FIRAS to generate a multi-component dust model that predicts the thermal emission at CMB frequencies with an angular resolution of 6 arcminutes. We apply the ACBAR filtering to the predicted dust maps for 150 GHz, and find the expected RMS to be at the μK level. Assuming the ACBAR maps contain the FSD dust templates with amplitudes parametrized by the quantity ξ, the observed maps T can be written as the sum $T_{CMB} + \xi T_{FSD}$. After cross-correlating the dust template maps T_{FSD} with the observed maps, we find that the Galactic dust is undetectable in the ACBAR 150 GHz data. The 1-σ upper limit on the amplitude parameter is $\xi < 2.6$, consistent with the FSD predictions (*i.e.*, $\xi = 1$). As in the case for the radio source flux measurements, the uncertainty in ξ is dominated by the CMB primary anisotropies. Therefore, dust with the morphology of the FSD maps does not significantly contribute to the observed anisotropy power. Nonetheless, the reported band-powers are calculated with the dust template mode projected out in each of the fields.

Dust emission from high redshift star forming galaxies can be a significant foreground contaminant in millimeter wavelength CMB maps. Recent observations with SCUBA/JCMT (Smail et al. 2002; Chapman et al. 2002; Borys et al. 2003), Bolocam/CSO (Laurent et al. 2005), and MAMBO/IRAM (Greve et al. 2004), provide constraints on both the source counts and the spectral dependence of these proto-galaxies. However, despite the tremendous progress made in studying these sources, their contributions at 150 GHz are still highly uncertain. The uncertainties come from the low number statistics in source counts and spectral dependence, difficulties in modeling the survey bias and completeness, and poorly studied angular correlations. In the absence of more decisive measurements, such as might be produced by the ongoing SHADES[11] survey and the BLAST[12] experiment, we ignore the clustering noise component and estimate the Poisson contribution from these proto-galaxies at the ACBAR observing frequencies.

The SCUBA results constrain the 850μm source counts with an uncertainty of $\sim 40\%$. There are considerable uncertainties in extrapolating this result to lower frequencies because the process depends not only on the dust properties, but also on the cosmic star formation history and the source evolution. Observations carried out at two different wavelengths, 1.2 mm with MAMBO, and 1.1 mm with Bolocam, can potentially provide this extrapolation phenomenologically. Greve et al. (2004) find that the MAMBO and SCUBA source counts agree if the MAMBO counts are scaled up in flux by a factor of 2.5, corresponding to a spectral dependence of $S_\nu \propto \nu^{2.65}$. We scale the fit for the SCUBA source count results (Borys et al. 2003) to 150 GHz (2 mm) according this spectral dependence. Using the formulae given in Scott & White (1999), we find the contribution of these sources to the CMB power spectrum at 150 GHz to be $\mathcal{D}_\ell \sim 37(\ell/2500)^2 \mu\mathrm{K}^2$. Since most of this fluctuation power comes from sources with fluxes between 0.1 and 10 mJy, the result is insensitive to a flux cut-off greater than 10 mJy. The Bolocam team (Laurent et al. 2005) found fewer sources at 1.1 mm than MAMBO did at 1.2 mm, implying a steeper spectrum for the sources. A fluctuation analysis of the same data also suggested lower source counts, especially for fluxes < 1mJy (Maloney et al. 2005). From Figure 15 of Laurent et al. (2005), we estimate the spectra between 850 μm and 1.1 mm to scale as $S_\nu \propto \nu^4$. Compared with the $37\mu\mathrm{K}^2$ at $\ell = 2500$ from the MAMBO/SCUBA extrapolation, which is just below the instrumental noise of ACBAR, the Bolocam/SCUBA model results in a negligible value of $4\mu\mathrm{K}^2$. Future sub-millimeter and millimeter observations are needed to fully characterize the properties of these sources. In the interpretation of the ACBAR data, we cautiously assume that the high-ℓ band-powers are not significantly contaminated by high redshift proto-galaxies.

[11] http://www.roe.ac.uk/ifa/shades/

[12] http://chile1.physics.upenn.edu/blastpublic/

Table 2
Millimeter Bright PMN Sources

Source Name/Position	Field	$S_{4.85}$ (mJy)	S_{150} (mJy)	$\alpha_{150/4.85}$
PMN J0455-4616*	CMB2	1653	2898 ± 60	0.15
PMN J0451-4653	CMB2	541	360 ± 58	-0.13
PMN J0439-4522	CMB2	634	383 ± 73	-0.16
PMN J0514-4554	CMB2	422	197 ± 68	-0.23
PMN J0515-4556	CMB2	990	524 ± 65	-0.20
PMN J0253-5441*	CMB5	1193	1799 ± 66	0.11
PMN J0210-5101*	CMB6	3198	1268 ± 86	-0.28
PMN J0214-5054	CMB6	61	186 ± 63	0.31
PMN J2235-4835*	CMB7	1104	656 ± 63	-0.16

Note. — These sources from the PMN 4.85 GHz catalog are detected at $> 2.8\sigma$ significance with ACBAR, corresponding to a false detection rate of 1. The fluxes at 4.85 GHz ($S_{4.85}$, from Wright et al. (1994)) and 150 GHz (S_{150}, measured by ACBAR) are given. The spectral index α is defined as $S_\nu \propto \nu^\alpha$. The uncertainties associated with S_{150} are dominated by the CMB fluctuations. The central guiding quasars (one in each of the 4 fields) are marked with asterisks (*). These sources, as well as the undetected PMN sources, are projected out from the data using the methods described by K04 and do not contribute to the power spectrum measurements reported in this paper.

6. RESULTS AND DISCUSSIONS

6.1. *Power Spectrum*

Applying the analysis method described in the previous sections to the ACBAR 2001 & 2002 150 GHz data leads to the power spectrum shown in Figure 1. A comparison with other recent CMB results is shown in Figure 3. The model curves in both figures are the "WMAP3+ACBAR" best fit model. We report the decorrelated band-powers, since the description of their statistical properties requires fewer parameters. Plotting the decorrelated band-powers also simplifies the visual comparison between models and the measurements. The decorrelation transformations are defined according to Tegmark (1997). The same transformations are applied to the window functions, which convert a model C_ℓ to the theoretical band-powers (Knox 1999). Following K04, we use the offset lognormal functions (Bond et al. 2000) to fit the likelihood functions, and report the fit parameters $\mathbf{q}, \sigma, \mathbf{x}$ for each band. The band-powers, uncertainties, and lognormal offsets are given in Table 3; this information along with the corresponding window functions are available for download from the ACBAR website [13].

The ACBAR data are consistent with the results of other CMB experiments, and fit the model predictions for a flat, Λ-dominated universe with a low baryon density. A narrow peak is clearly seen in the power spectrum at $\ell \sim 820$, corresponding to the third harmonic of the acoustic oscillations in the early universe. This detection is in agreement with previous detections of this feature by BOOMERANG (Jones et al. 2006) and further confirms the coherent origin of the cosmic perturbations (Albrecht et al. 1996). Despite the nearly exponential damping at the high-ℓ, the primary CMB fluctuations are detected with a signal-to-noise ratio of greater than 4 up to $\ell = 2000$. The photon diffusion mechanism predicted at high-ℓ is verified to a high degree of accuracy.

6.2. *Anisotropies at $\ell > 2000$*

Various theoretical models predict that the secondary anisotropy induced by the thermal SZ effect in clusters of galaxies begins to dominate over primary anisotropy at $\ell \gtrsim 2000$ for standard cosmological parameters (Cooray et al. 2000; Komatsu & Seljak 2002). The level of the signal is extremely sensitive to the normalization of the the matter power spectrum, usually parameterized by the present-day RMS mass fluctuation on 8 h^{-1} Mpc scales, σ_8. The SZ effect has a clear spectral signature. In the nonrelativistic limit, the thermodynamic temperature difference from SZ effect (ΔT_{SZ}) is given by

$$\frac{\Delta T_{SZ}}{T_{CMB}} = y\left(x\frac{e^x+1}{e^x-1} - 4\right), \quad (6)$$

where $x = \frac{h\nu}{kT_{CMB}} = \nu/56.8\,\mathrm{GHz}$. The quantity y is known as the Compton parameter and is proportional to the integrated electron density along the line of sight through the cluster (*e.g.*, Peacock (1999)). The CBI Deep field observations at 30 GHz detect power on scales corresponding to $\ell > 2000$ in excess of the predicted primary CMB anisotropy. This "excess power" has been interpreted as the SZ effect produced by intervening galaxy clusters (Mason et al. 2003; Readhead et al. 2004a; Bond et al. 2005). On the other hand, a variety of models including non-standard primordial effects have also been proposed as possible explanations (Griffiths et al. 2003; Subramanian et al. 2003). The unique photon emission spectrum of the thermal SZ effect distinguishes it from these alternative explanations for the observed anisotropy.

The ACBAR band powers corresponding to the smallest angular scales lie slightly above the best fit WMAP3 ΛCDM model. The four highest ℓ bins jointly produce an excess of $51 \pm 42 \mu\mathrm{K}^2$ after the model primary power spectrum is subtracted. The combination of this result with measurements at lower frequencies can be used to constrain the photon emission spectrum of the excess, shed-

[13] http://cosmology.berkeley.edu/group/swlh/acbar/index.html

ding light on its origin. We perform a joint analysis of the CBI results and the new ACBAR data at $\ell > 2000$, assuming the contributions from primary anisotropy are known. In each experiment, the theoretical band-powers for primary anisotropy are calculated from the product of the ΛCDM power spectrum and band window functions, which are then subtracted from the observed band-powers. A two-dimensional likelihood function is calculated from these excess band-powers and their uncertainties, where the two parameters are the ratio of the 30 GHz and 150 GHz excess, ζ, and the power at 30 GHz, σ_{30}^2 (in μK_{CMB}^2). We then marginalize over the σ_{30}^2 parameter and plot the likelihood function for the power ratio ζ in Figure 4. Since ACBAR measures significantly less power at 150 GHz, the data disfavor sources that result in a blackbody spectrum (*i.e.*, $\zeta = 1$). Using the ACBAR and CBI frequency response and equation (6), we calculate the power ratio $\zeta = 4.3$ for the thermal SZ effect. From the likelihood plot, we conclude that it is 4.5 times more likely that the excess seen by CBI and ACBAR is the result of the thermal SZ effect ($\zeta = 4.3$) than a primordial process ($\zeta = 1$). Since the expected ratio of flux at 30 GHz to 150 GHz from radio sources is expected to be <0.1, such sources are disfavored as being responsible for the excess power seen by CBI at about the same significance ($\sim 1.2\sigma$) with which ACBAR detects excess power. Additional data from ACBAR or other higher frequency instruments will be required to make a definitive statement about the origin of the excess power seen by CBI and BIMA.

7. COSMOLOGICAL PARAMETERS

In this section, we estimate cosmological parameters for a minimal inflation-based, spatially-flat, tilted, gravitationally lensed, ΛCDM model characterized by six parameters, and then investigate models including extra parameters to test extensions of the theory. For our base model, the six parameters are: the physical density of baryonic and dark matter, $\Omega_b h^2$ and $\Omega_c h^2$; a constant spectral index n_s and amplitude $\ln A_s$ of the primordial power spectrum, the optical depth to last scattering, τ; and the ratio of the sound horizon at last scattering to the angular diameter distance, θ. The primordial comoving scalar curvature power spectrum is expressed as $\mathcal{P}_s(k) = A_s(k/k_n)^{(n_s-1)}$, where the normalization (pivot-point) wavenumber is chosen to be $k_n = 0.05\,\mathrm{Mpc}^{-1}$. The parameter θ maps angles observed at our location to comoving spatial scales at recombination; changing θ shifts the entire acoustic peak/valley and damping pattern of the CMB power spectra. Additional parameters are derived from the basic set. These include: the energy density of a cosmological constant in units of the critical density, Ω_Λ; the age of universe; the energy density of non-relativistic matter, Ω_m; the *rms* (linear) matter fluctuation in $8h^{-1}$Mpc spheres, σ_8; the redshift to reionization, z_{re}; and the value of the present day Hubble constant, H_0, in units of $\mathrm{kms}^{-1}\mathrm{Mpc}^{-1}$. Tilted primordial spectra indicate the presence of a tensor-induced anisotropy component, however, we do not include this potential contribution due to its uncertain amplitude. The influence of the tensor component would only be significant at low-ℓ, not in the regime which ACBAR probes. We also restrict this work to flat ΛCDM models, motivated by the observed curvature being so close to zero. However, we have run models with non-zero curvature Ω_K, and find that they reproduce the standard geometrical degeneracy associated with Ω_K and Ω_Λ.

We have also considered two extensions to the basic model which could potentially impact the interpretation of the ACBAR bandpowers. These extended models include flat ΛCDM models with a running scalar spectral index characterized by the derivative $dn_s/d\ln k(k_n)$, and flat ΛCDM models with a Sunyaev-Zel'dovich contribution to the angular power spectrum with amplitude parametrized by α^{SZ}. We also investigate a model where both a running spectral index and a SZ contribution are considered simultaneously.

The parameter constraints are obtained using a Monte Carlo Markov Chain (MCMC) sampling of the multi-dimensional likelihood as a function of model parameters. Our software is based on the publicly available CosmoMC[14] package (Lewis & Bridle 2002). CMB angular power spectra and matter power spectra are computed using the CAMB code (Lewis et al. 2000). We approximate the full non-Gaussian bandpower likelihoods with an offset lognormal distribution (Bond et al. 2000) found by explicit fits (see K04 for a detailed discussion of the calculation). Our standard CosmoMC results include the effects of weak gravitational lensing on the CMB (Seljak 1996; Lewis et al. 2000). Lensing effects in the temperature spectrum are expected to become significant at scales $\ell > 1000$, hence it is important to include this effect when interpreting the ACBAR results. The major effect of lensing is a scale-dependent smoothing of the angular power spectrum which diminishes the peaks and valleys of the spectrum. Inclusion of lensing in the model improves the fit to the data for all experiment combinations. However, we find that the parameter mean values and uncertainties are largely unaffected by the inclusion of lensing with some exceptions, in particular the introduction of lensing tends to increase the value of σ_8.

The typical computation consists of 8 separate chains, each having different initial random parameter choices. The chains are run until the largest eigenvalue of the Gelman-Rubin test is smaller than 0.1 after accounting for burn-in. Uniform priors with very broad distributions are assumed for the basic parameters. The standard run also includes a weak prior on the Hubble constant ($45 < H_0 < 90$ km s^{-1} Mpc^{-1}) and on the age of the universe (> 10 Gyrs). We also investigate the influence of adding Large Scale Structure (LSS) data from the 2 degree Field Galaxy Redshift Survey (2dFGRS) (Cole et al. 2005) and the Sloan Digital Sky Survey (SDSS) (Tegmark et al. 2004). When including the LSS data, we use only the band powers for length scales larger than $k \sim 0.1h\mathrm{Mpc}^{-1}$ to avoid non-linear clustering and scale-dependent galaxy biasing effects. We marginalize over a parameter b_g^2 which describes the (linear) biasing of the galaxy-galaxy power spectrum for $L_\star$ galaxies relative to the underlying mass density power spectrum. We adopt a Gaussian prior on b_g^2 centered around $b_g = 1.0$ with a conservative width equivalent to $\delta b_g = 0.3$; all parameters except σ_8 and τ are insensitive to this width.

[14] http://cosmologist.info/cosmomc

7.1. *Base Parameters Results*

The results for the basic flat tilted ΛCDM parameters are shown in Table 4. The confidence limits are obtained by marginalizing the multi-dimensional likelihoods down to one dimension. The median value is obtained by finding the 50% integral of the resulting likelihood function while the lower and upper error limits are obtained by finding the 16% and 84% integrals respectively. The CMBall data combination includes: the ACBAR results presented here; the WMAP 3 year TT, TE, and EE spectra, with the EE not included at higher ℓ as in Hinshaw et al. (2006); the CBI extended mosaic results (Readhead et al. 2004a) and polarization results (Readhead et al. 2004b; Sievers et al. 2005), combined in the manner described in Sievers et al. (2005);[15] the DASI two year results (Halverson et al. 2002); the DASI EE and TE bandpowers (Leitch et al. 2005); the VSA final results (Dickinson et al. 2004); the MAXIMA 1998 flight results (Hanany et al. 2000); and the TT, TE, and EE results from the BOOMERANG 2003 flight (Jones et al. 2006; Piacentini et al. 2006; Montroy et al. 2006). Only $\ell > 350$ bandpowers are included for BOOMERANG because of overlap with WMAP3 (although inclusion of the lower ℓ results leaves the parameter results essentially unchanged). While ACBAR and BOOMERANG are both calibrated through WMAP, this is a small contribution to the total uncertainty in the ACBAR calibration and we treat the calibration uncertainties as independent in our parameter analysis. Although the DASI, CBI and BOOMERANG 2003 EE and TE results for high ℓ polarization are included, they have little impact on the values of the parameters we obtain.

In all our runs we have used the updated WMAP3 likelihood code (http://lambda.gsfc.nasa.gov/) which includes an updated point-source correction *cf.* Huffenberger et al. (2006) and foreground marginalization on large angular scales. These updates result in a small increase in the Ω_m and σ_8 values compared to those reported in Spergel et al. (2006).

The results for the basic model parameter set with various combinations of data are summarized in Fig. 5. The most striking feature of the results is that the solutions determined from WMAP3 alone are quite compatible with the extension by ACBAR (and that of the other data) to higher ℓ. This consistency means that the additional CMB data (including ACBAR) have little impact on the cosmological parameters determined by WMAP3. We have tested the effect of a significantly smaller ACBAR calibration error, such as we anticipate for the final ACBAR release. We find a much larger impact on the parameter values and errors; the values are similar to those found for CMBall+LSS.

With the original Spergel et al. (2006) WMAP3 likelihood code, there was a shift in σ_8 and Ω_m to higher values when additional data was included. However, with the updated WMAP3 likelihood code, the addition of the ACBAR and CMBall bandpowers leads to essentially no shift in σ_8 and Ω_m; however, including the LSS data does still result in a slight increase in these parameters. The new likelihood code corrects the lower power in the third acoustic peak which was leading to low values for σ_8 and $\Omega_m h^2$.

The comoving damping scale, determined as a derived cosmological parameter using only the ACBAR and WMAP3 data is $R_D = 10.5 \pm 0.2\,\mathrm{Mpc}^{-1}$. The corresponding angular scale is $\ell_D = 1355^{+5}_{-5}$. These values for R_D and ℓ_D are in excellent agreement with values obtained using earlier datasets (Bond et al. 2003). We also find the comoving sound crossing distance is $R_s = 147.8^{+2.3}_{-2.3}\,\mathrm{Mpc}^{-1}$, with a corresponding angular scale $\ell_s = 100/\theta = 95.9^{+1.0}_{-0.2}$, in agreement with the value for θ in Table 4.

Inclusion of lensing in our standard parameter runs increases the best-fit model likelihoods in all cases. The difference between the log likelihoods of the lensed and non–lensed models for the WMAP3 run is $\Delta \ln L = 0.86$. The log likelihood difference increases to 1.7 with ACBAR included, 2.46 with CMBall, and 3.69 for the CMBall+LSS data combination. The mean values of the parameters do not shift significantly with the inclusion of lensing; for example, σ_8 increases from 0.778 to 0.788 for the CMBall data set and from 0.804 to 0.813 for CMBall+LSS. The best-fit $\mathcal{D}_\ell$'s for the lens and no-lens cases look quite similar, but the subtle smoothing of the peaks and troughs by lensing results in a better fit to the the data for each combination of experiments.

7.2. *Running Spectral Index*

The first release of WMAP data showed evidence for running of the CMB power spectrum spectral index, particularly when combined with measurements of LSS (Spergel et al. 2003). Extending the basic model to allow for running of the spectral index around the pivot point $k_\star = 0.05\mathrm{Mpc}^{-1}$ yields $dn_s/d\ln k(k_\star) = -0.053^{+0.031}_{-0.029}$ for WMAP3 only. The tendency for negative running indices is due mostly to the low ℓ end, where the multipoles are lower than the standard ΛCDM model. The contribution from the high ℓ end is less significant. Since the WMAP3 results extend to reasonably high ℓ, the addition of the ACBAR results shifts the constraints only marginally $dn_s/d\ln k(k_\star) = -0.045^{+0.026}_{-0.026}$. The effect of adding the ACBAR data can be seen most clearly in Fig. 7 which shows the correlation between n_s and $dn_s/d\ln k$. The central value is similar, but the errors are further reduced with the CMBall + LSS combination, $dn_s/d\ln k(k_\star) = -0.047^{+0.021}_{-0.021}$. Similar to the results from WMAP1 and earlier versions of the CMBall data set (Bond et al. 2003; MacTavish et al. 2006), a negative running is still favored at about the 2-σ level by each of the data combinations considered. The models including running favor significantly lower values of the scalar spectral index, $n_s = 0.903^{+0.029}_{-0.028}$. However this result depends on the choice of pivot point $k_\star$: a smaller value would yield a higher result while a higher one would give an even lower result.

7.3. *Sunyaev-Zel'dovich template extension*

As described in Section 6.2, fluctuations from the thermal Sunyaev-Zel'dovich (SZ) effect are expected to dominate over the damped primordial contributions to the CMB anisotropy at multipoles beyond $\ell \sim 2500$. The

[15] We exclude the band powers below $\ell = 600$ from the CBI extended mosaic results to reduce the correlation with the TT band powers of the CBI polarization dataset which influence the sample-dominated end of the spectrum.

magnitude of the SZ signal depends strongly on the overall matter fluctuation amplitude, σ_8. We have modified our parameter fitting pipeline to allow for extra frequency dependent contributions to the CMB power spectrum and have implemented it in a simple analysis using a fixed template $\hat{\mathcal{C}}_\ell^{\rm SZ}$ for the shape of the thermal SZ power spectrum. The template was obtained from large hydrodynamical simulations of a scale-invariant ($n_s = 1$) ΛCDM model with $\sigma_8 = 0.9$ and $\Omega_b h = 0.029$. (See Bond et al. (2005) for a detailed description of the simulations.) Recently the WMAP team have used a different SZ template based on analytic estimations of the power spectrum (Spergel et al. 2006). It is characterized by a slower rise in ℓ than the simulation-based one, which cut nearby clusters out of the power spectrum. There has been no fine-tuning of the spectra to agree with all of the X-ray and other cluster data. This may have an effect on shape, especially at high ℓ.

We add an SZ contribution $\mathcal{C}_\ell^{\rm SZ} = (\alpha^{\rm SZ})^2 \hat{f}_\nu \mathcal{C}_\ell^{\rm SZ}$ to the base six parameter model spectrum. Here f_ν is the frequency-dependent SZ pre-factor and $\alpha^{\rm SZ} = \sigma_8^{7/2}(\Omega_b h/0.029)$ is a scaling factor determined from hydrodynamical simulations. We consider two cases: (1) the scaling parameter $\alpha^{\rm SZ}$ is slaved to $\sigma_8^{7/2}(\Omega_b h/0.029)$; (2) $\alpha^{\rm SZ}$ is allowed to float freely. Including this SZ template with all parameters varying is complementary to the analysis of § 6.2 which directly compared the residual CBI and ACBAR bandpowers in the excess region. In that more restrictive analysis, the primary power spectrum is fixed and f_ν is allowed to vary as well as a broad-band excess power. We found that the spectrum of the excess was compatible with the SZ effect, motivating the SZ-restricted study considered here.

Regardless of the data combination, we find that including an SZ component in the model has little effect on the determination of the basic cosmological parameters. This can be seen by comparing Table 5 with Table 4. We also find that it has little effect, whether $\alpha^{\rm SZ}$ is related to cosmic parameters through $\alpha^{\rm SZ} = \sigma_8^{7/2}(\Omega_b h/0.029)$ or is allowed to float freely. Note that the SZ results break the $A_s e^{-2\tau}$ near-degeneracy (as does weak lensing, though not as strongly.)

We begin with the combination of the ACBAR and WMAP3 data. When $\alpha^{\rm SZ}$ is allowed to float freely, we obtain $\alpha^{\rm SZ} = 0.57^{+0.20}_{-0.56}$. We can use the above definition to map the floating SZ amplitude parameter $\alpha^{\rm SZ}$ to a corresponding $\sigma_8^{\rm (SZ)} = 0.84^{+0.15}_{-0.23}$. The low significance of excess power in the ACBAR data results in weak constraints on $\sigma_8^{\rm SZ}$, particularly for the lower limit. We have not tabulated the results for the slaved $\alpha^{\rm SZ}$ case since it results in extremely small changes in σ_8. For example, fits to the ACBAR+WMAP3 band powers give $\sigma_8 = 0.77^{+0.05}_{-0.05}$ when we include the SZ contribution in the model, and $\sigma_8 = 0.78^{+0.05}_{-0.05}$ when we ignore it.

When the high ℓ bandpowers of CBI and BIMA are included in the analysis, there is a significant detection of excess power. Both the CBI and BIMA bandpowers are from 30 GHz interferometric observations and have higher f_ν values than ACBAR. For the slaved case, the errors tighten slightly while the central value remains stationary with $\sigma_8 = 0.79^{+0.04}_{-0.04}$. For the floating case we find $\alpha^{\rm SZ} = 0.79^{+0.06}_{-0.09}$ which maps to $\sigma_8^{\rm (SZ)} = 0.92^{+0.05}_{-0.06}$.

The CMBall + BIMA combination results in uncertainties for $\sigma_8^{\rm (SZ)}$ which are comparable to those of σ_8. A visual summary of the results is shown in Fig. 8 where we plot both σ_8 and $\sigma_8^{\rm (SZ)}$ against the spectral index for a number of data combinations. It is interesting to note that the tension between σ_8 and $\sigma_8^{\rm (SZ)}$ is relaxed by the inclusion of the LSS data which increases the value of σ_8. We caution, however, that the fit depends on the SZ template shape and its extension into the higher ℓ regime probed by BIMA. This analysis assumes that no additional foreground sources, such as dusty proto-galaxies, contribute significantly to the observed anisotropy. [16] It is worth mentioning that the baseline lensed model for the CMB continues to be a better fit to the data regardless of the inclusion of the SZ extension. The decrease in log likelihood for the fit to the model including SZ, when lensing is taken into account, is $\Delta \ln L = 2.06$ for CMBall+BIMA and $\Delta \ln L = 2.38$ for CMBall+BIMA+LSS. We also find that neglecting lensing in the model tends to increase the existing tension between the derived σ_8 and σ_8^{SZ} values.

We find that including the SZ template and running spectral index simultaneously selects a more negative running index due to the greater downturn in high ℓ power. For example, with the CMBall + BIMA + LSS combination we get $dn_s/d\ln k = -0.60^{+0.022}_{-0.021}$ compared with the no-SZ result $dn_s/d\ln k = -0.47^{+0.021}_{-0.021}$. In either case, the excess power leads to $\sigma_8^{\rm (SZ)} = 0.92^{+0.04}_{-0.06}$, virtually unchanged from the results for the model without running.

8. CONCLUSIONS

We have measured the CMB angular power spectrum up to multipole values of $\ell \sim 3000$ using the complete data set from the 2001 and 2002 ACBAR 150 GHz observations. The data are analyzed with a refined method in which the band-powers are calculated from un-differenced maps. We calibrate the data by comparing the flux of the galactic HII region RCW38 in the overlapped region of ACBAR and BOOMERANG; the flux scale of BOOMERANG is calibrated through comparison with WMAP. The new calibration is found to be consistent with the previous planet-based calibration, but with uncertainty reduced from 10% to 6.0% in temperature.

We have carried out various jackknife tests to show that the ACBAR band-powers are not compromised by systematic errors. In deriving the power spectrum, we have projected out known foreground modes including the FSD dust template and the PMN radio sources, however, these projections have no significant effect on the final band-powers. The contribution to temperature fluctuations at 150 GHz from high redshift dusty protogalaxies remains uncertain. However, extrapolating from recent observations near 270 GHz, we determine that these sources are unlikely to contribute significantly to the ACBAR band-powers.

The band-powers presented in Table 3 are the most sensitive measurements of the CMB temperature anisotropy

[16] We note that the non-Gaussian nature of the SZ signal is included in the BIMA results but was not taken into account in the CBI analysis. The effect of the sample variance tends to open up the allowed range towards lower σ_8 values (Goldstein et al. 2003; Readhead et al. 2004a).

to date in the range of $1000 \lesssim \ell \lesssim 3000$. The power spectrum continues to support a spatially flat ΛCDM cosmology, with a low baryonic density. Since the WMAP3 data now extends into the third peak, the addition of the damping tail data from ACBAR results in only minor changes in the values and uncertainties of the standard cosmological parameters. For all combinations of data we have considered beyond WMAP3 alone, the baseline lensed CMB model results in significantly better fits than models neglecting lensing.

The ACBAR data has also been used to place interesting constraints on secondary anisotropies. The band-powers for $\ell > 2000$ are significantly smaller than those reported by the CBI and BIMA experiments and provide only a suggestion (1.2σ) of excess power above what is expected from primary CMB anisotropy (§ 6.2). The excess power has a frequency spectrum consistent with the thermal SZ effect and inconsistent with thermal sources such as primary anisotropy. Because of the weak detection of excess power by ACBAR, radio sources are slightly disfavored as the source of the signal, but cannot be ruled out.

Theoretical work suggests that the thermal SZ effect should be the dominant source of secondary anisotropy. The expected amplitude of the thermal SZ effect is extremely sensitive to σ_8. Adding the SZ amplitude to our cosmological parameter runs, we infer values for $\sigma_8^{(SZ)}$ that are somewhat higher than the σ_8 found from the standard parameter runs, but consistent within the uncertainties. This tension is further reduced when LSS data is included in the parameter runs.

The results presented here are derived from a subset of the total ACBAR data set which is currently being analyzed. The final ACBAR power spectrum at 150 GHz will include 3.7 times more effective integration time, 6.7 times more sky coverage, and a direct calibration from comparison with WMAP3. This will result in significantly reduced uncertainties across the entire power spectrum and improved constraints on standard cosmological parameters as well as secondary anisotropies.

The ACBAR program has been primarily supported by NSF office of polar programs grants OPP-8920223 and OPP-0091840. This research used resources of the National Energy Research Scientific Computing Center, which is supported by the Office of Science of the U.S. Department of Energy under Contract No. DE-AC03-76SF00098. Chao-Lin Kuo acknowledges support from a NASA postdoctoral fellowship and Marcus Runyan acknowledges support from a Fermi fellowship. Christian Reichardt acknowledges support from a National Science Foundation Graduate Research Fellowship. We thank members of the BOOMERANG team, in particular Brendan Crill, Bill Jones, and Tom Montroy for providing access to the B03 data, the pipeline used to generate simulation maps, and assistance with its operation.

APPENDIX

A. CALIBRATION

The calibration used for the first ACBAR data release was obtained by observations of Venus and Mars, as detailed in Runyan (2002). In this section, we describe a new calibration based on the comparison of B03 and ACBAR observations of the galactic HII region RCW38. B03 was calibrated by an a_{lm}-based comparison of CMB structure with WMAP in the region of B03 sky coverage with a 1.8% uncertainty (Jones et al. 2006). The B03-ACBAR cross-calibration method is described below, with a detailed accounting of uncertainty in Table A6.

BOOMERANG-ACBAR Cross Calibration ACBAR made daily high signal-to-noise maps of the galactic source RCW38. B03 also mapped portions of the galactic plane including RCW38 (Fig. A.0.0.0), allowing a direct comparison of the high signal-to-noise maps made by the two experiments. The experiments have different scan patterns, beam widths, and spatial filters that can effect the measured flux. We resample the B03 map using pointing information for each ACBAR observation to generate an ACBAR-equivalent B03 observation. The ACBAR maps are smoothed to simulate the effect of Boomerang's larger beam. Large spatial modes in both experiments are corrupted; in ACBAR by chopper-synchronous offsets and in B03 by the high-pass filter. We simultaneously fit a quadratic offset and Gaussian source model from each scan of the ACBAR and B03 maps which removes these modes without affecting the amplitude of a point source. After coadding the channel maps, we integrate the flux within a $18'$ radius of the source. The integrated flux is robust to small misestimates or changes in the beam size. The measured flux ratio and the associated uncertainties are listed under *Ratio of B03 over ACBAR* in Table A6.

We use Monte Carlo techniques to estimate the transfer function of this method. Using a model of RCW38 and its surroundings, we generate simulated timestreams for the observations with each experiment. Maps are created from the timestreams and are filtered as described above. The ratio of the transfer functions is found to be $ACBAR/B03 = 1.056 \pm 0.002$. We have tested the dependence of the transfer function on the assumed signal template and include a 3% uncertainty in our calibration due to this effect. This technique is readily adapted to include the effect of the beam uncertainty for each experiment and we find that the beam contributes 1.35% to our estimated uncertainty. The effect of the transfer function and the associated uncertainty are listed under *Transfer Function* in Table A6.

RCW38 has a much different spectrum than the CMB, and the effective CMB temperature difference it produces depends on the photon-frequency. The calibration described here is based on observations with ACBAR's 150 GHz channels and Boomerang's 145 GHz channels which have similar bandpasses (Fig. A.0.0.0). We account for the small difference in bandpass by convolving the measured spectral response of each experiment with a model of RCW38's spectrum from (Masi et al. 2006). If two maps nominally calibrated in CMB temperature units are integrated about RCW38, the true

TABLE 3
JOINT LIKELIHOOD BAND-POWERS

ℓ range	l_{eff}	q (μK^2)	σ (μK^2)	x (μK^2)
351-550	428	2680	284	-698
551-650	605	2225	280	-218
651-750	700	2018	227	-286
751-850	804	2796	276	-509
851-950	910	1662	174	-257
951-1050	1003	1282	132	-111
1051-1150	1102	1284	124	-146
1151-1250	1204	1116	108	-40
1251-1350	1303	877	92	-43
1351-1450	1403	782	89	63
1451-1550	1502	563	73	118
1551-1650	1601	524	70	139
1651-1750	1703	351	62	266
1751-1875	1810	254	54	272
1876-2025	1943	294	57	307
2026-2175	2096	278	74	520
2176-2325	2242	59	68	508
2326-2500	2395	196	100	851
2501-3000	2607	190	120	1625

Note. — Band multipole range and weighted value ℓ_{eff}, decorrelated band-powers q_B, uncertainty σ_B , and log-normal offset x_B from the joint likelihood analysis of CMB2, CMB5, CMB6 and CMB7. The PMN radio point source and IRAS dust foreground templates have been projected out in this analysis.

TABLE 4
BASIC 6 PARAMETER CONSTRAINTS

	WMAP3	WMAP3 + ACBAR	CMBall	CMBall+LSS
$\Omega_b h^2$	$0.0226^{+0.0008}_{-0.0007}$	$0.0225^{+0.0007}_{-0.0007}$	$0.0226^{+0.0006}_{-0.0006}$	$0.0226^{+0.0006}_{-0.0006}$
$\Omega_c h^2$	$0.108^{+0.008}_{-0.009}$	$0.108^{+0.008}_{-0.007}$	$0.110^{+0.006}_{-0.006}$	$0.115^{+0.005}_{-0.005}$
θ	$1.042^{+0.004}_{-0.004}$	$1.042^{+0.004}_{-0.003}$	$1.042^{+0.003}_{-0.003}$	$1.042^{+0.003}_{-0.003}$
τ	$0.097^{+0.012}_{-0.014}$	$0.092^{+0.014}_{-0.014}$	$0.092^{+0.013}_{-0.014}$	$0.090^{+0.013}_{-0.013}$
n_s	$0.966^{+0.017}_{-0.017}$	$0.964^{+0.016}_{-0.015}$	$0.963^{+0.016}_{-0.014}$	$0.960^{+0.015}_{-0.014}$
$\log[10^{10} A_s]$	$3.05^{+0.08}_{-0.06}$	$3.05^{+0.06}_{-0.07}$	$3.05^{+0.06}_{-0.06}$	$3.07^{+0.05}_{-0.06}$
Ω_Λ	$0.75^{+0.03}_{-0.03}$	$0.76^{+0.03}_{-0.04}$	$0.75^{+0.03}_{-0.03}$	$0.72^{+0.03}_{-0.03}$
Age $[Gyrs]$	$13.7^{+0.2}_{-0.1}$	$13.7^{+0.2}_{-0.1}$	$13.7^{+0.1}_{-0.1}$	$13.7^{+0.1}_{-0.1}$
Ω_m	$0.25^{+0.03}_{-0.03}$	$0.24^{+0.04}_{-0.03}$	$0.25^{+0.03}_{-0.03}$	$0.28^{+0.03}_{-0.03}$
σ_8	$0.78^{+0.06}_{-0.05}$	$0.78^{+0.05}_{-0.05}$	$0.79^{+0.04}_{-0.04}$	$0.81^{+0.03}_{-0.03}$
$z_r e$	$11.8^{+2.7}_{-2.6}$	$11.5^{+2.3}_{-2.6}$	$11.6^{+2.2}_{-2.6}$	$11.5^{+2.2}_{-2.4}$
H_0	$72.7^{+3.0}_{-2.3}$	$72.9^{+3.1}_{-3.1}$	$72.3^{+2.8}_{-2.8}$	$70.4^{+2.3}_{-2.2}$

Note. — Results for the basic parameter set. The runs all assumed flat cosmologies, uniform and broad priors on each of the basic six parameters and a weak prior on the Hubble constant ($45 < H_0 < 90$ km s^{-1} Mpc^{-1}) and the age (> 10 Gyr). All runs included the effect of weak gravitational lensing on the spectra which is significant for the $\ell > 1000$ scales probed by ACBAR. The results are nearly identical if we include an SZ template, with the largest, but still relatively minor, impact on σ_8 and τ.

calibration factor **K** will depend on the measured flux ratio I_{B03}/I_{ACBAR}, the bandpass of each experiment t_ν, the spectrum of RCW38 S_ν^{RCW38} and the known blackbody spectrum of the CMB $\frac{dB_\nu}{dT}|_{T_{CMB}}$:

$$K = \frac{I_{B03}}{I_{ACBAR}} * R$$

$$\text{where } R = \frac{\int t_\nu^{ACBAR} \lambda^2 S_\nu^{RCW38} d\nu}{\int t_\nu^{B03} \lambda^2 S_\nu^{RCW38} d\nu} \frac{\int t_\nu^{B03} \lambda^2 \frac{dB_\nu}{dT}|_{T_{CMB}} d\nu}{\int t_\nu^{ACBAR} \lambda^2 \frac{dB_\nu}{dT}|_{T_{CMB}} d\nu}.$$

TABLE 5
SZ TEMPLATE PARAMETER CONSTRAINTS

	ACBAR+WMAP3	CMBall	CMBall+BIMA	CMBall+BIMA+LSS
$\Omega_b h^2$	$0.0224^{+0.0008}_{-0.0006}$	$0.0226^{+0.0007}_{-0.0006}$	$0.0226^{+0.0006}_{-0.0006}$	$0.0226^{+0.0006}_{-0.0006}$
$\Omega_c h^2$	$0.106^{+0.008}_{-0.007}$	$0.108^{+0.007}_{-0.006}$	$0.108^{+0.007}_{-0.006}$	$0.114^{+0.005}_{-0.005}$
θ	$1.041^{+0.004}_{-0.004}$	$1.042^{+0.003}_{-0.003}$	$1.042^{+0.003}_{-0.003}$	$1.042^{+0.003}_{-0.003}$
τ	$0.096^{+0.014}_{-0.014}$	$0.092^{+0.015}_{-0.014}$	$0.091^{+0.014}_{-0.014}$	$0.090^{+0.012}_{-0.012}$
$\alpha^{\rm SZ}$	$0.57^{+0.20}_{-0.56}$	$0.82^{+0.14}_{-0.81}$	$0.79^{+0.06}_{-0.09}$	$0.77^{+0.07}_{-0.08}$
n_s	$0.962^{+0.018}_{-0.016}$	$0.960^{+0.016}_{-0.015}$	$0.961^{+0.017}_{-0.014}$	$0.958^{+0.015}_{-0.015}$
$\log[10^{10} A_s]$	$3.05^{+0.06}_{-0.07}$	$3.04^{+0.06}_{-0.06}$	$3.04^{+0.07}_{-0.06}$	$3.06^{+0.06}_{-0.05}$
Ω_Λ	$0.76^{+0.03}_{-0.04}$	$0.75^{+0.03}_{-0.03}$	$0.76^{+0.03}_{-0.03}$	$0.73^{+0.02}_{-0.03}$
Age $[Gyrs]$	$13.7^{+0.2}_{-0.2}$	$13.7^{+0.1}_{-0.2}$	$13.6^{+0.1}_{-0.1}$	$13.7^{+0.1}_{-0.1}$
Ω_m	$0.24^{+0.04}_{-0.03}$	$0.25^{+0.03}_{-0.03}$	$0.24^{+0.03}_{-0.03}$	$0.27^{+0.03}_{-0.02}$
σ_8	$0.77^{+0.05}_{-0.05}$	$0.78^{+0.04}_{-0.04}$	$0.78^{+0.04}_{-0.04}$	$0.81^{+0.03}_{-0.03}$
z_{re}	$11.9^{+2.0}_{-2.5}$	$11.6^{+2.3}_{-2.7}$	$11.4^{+2.6}_{-2.4}$	$11.5^{+2.0}_{-2.4}$
$\sigma_8^{\rm SZ}$	$0.84^{+0.15}_{-0.23}$	$0.92^{+0.08}_{-0.15}$	$0.92^{+0.05}_{-0.06}$	$0.90^{+0.05}_{-0.07}$
H_0	$73.3^{+3.1}_{-3.1}$	$72.9^{+2.9}_{-2.9}$	$73.1^{+2.9}_{-2.9}$	$70.7^{+2.1}_{-2.1}$

Note. — Marginalized parameter constraints for the SZ template runs with independent amplitude. The SZ template contribution is scaled by a frequency dependent factor for each experiment and an independent amplitude $\alpha^{\rm SZ}$. The parameter $\sigma_8^{\rm SZ}$ is the normalization derived from $\alpha^{\rm SZ}$.

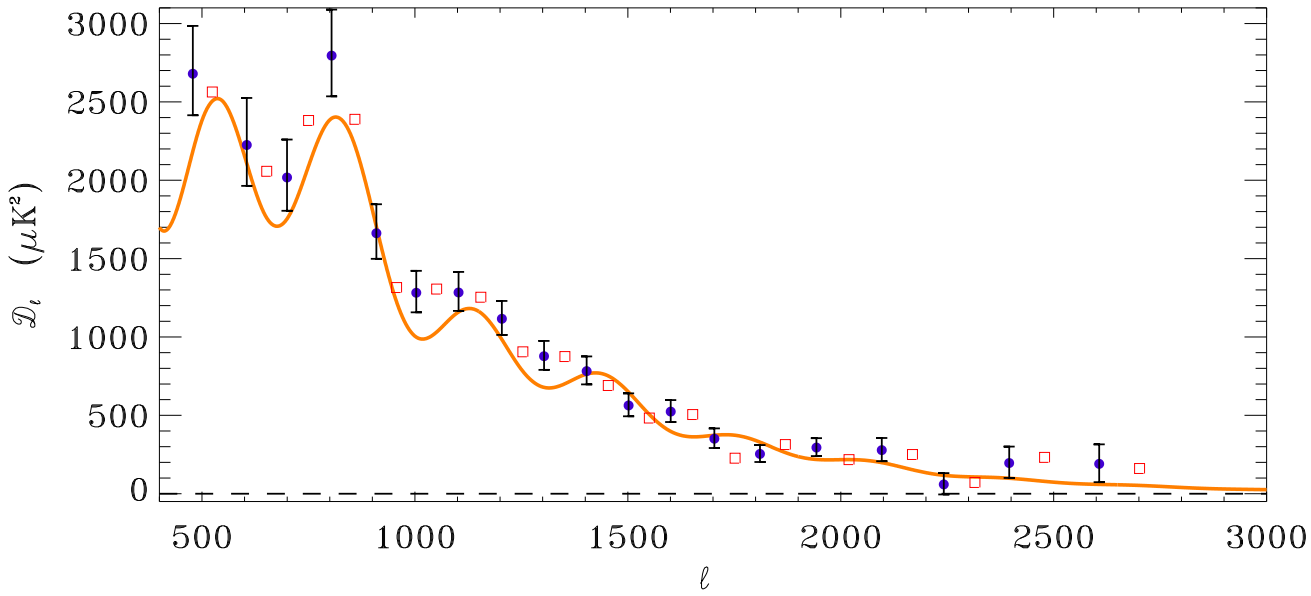

FIG. 1.— The de-correlated ACBAR band-powers for two alternate binnings. These two binnings are not independent, therefore only one set is shown with error bars, which correspond to 1-σ uncertainties calculated from the offset lognormal fits to the likelihood function. Both the overall features and the damping scale are in good agreement with predictions from a flat, low baryon density ΛCDM Universe. The third acoustic peak (around $\ell = 800$) is clearly seen. Small scale primary CMB fluctuations are detected with high signal-to-noise ratio (> 4) up to $l = 2000$. The plotted model line is the best fit to the WMAP3 and ACBAR bandpowers.

This factor R includes the full dependence of the calibration on RCW38's spectrum and the bandpasses of each experiment. The dominant source of uncertainty is RCW38's spectrum; to be conservative, we double the estimates listed in Masi et al. (2006). The model consists of two components: a power law term with $\alpha = 0.5 \pm 0.2$ and a dust term with $T_{dust} = 22.4 \pm 1.8$ K. Only the relative amplitude of the two terms is important: $A_{powerlaw@30\,GHz}/A_{dustpeak} = 867 \pm 400$. We also include uncertainty in the laboratory measurement of each experiment's bandpass. The mean value and uncertainty in R is estimated using 100,000 realizations of the above parameters, and found to be 1.008 ± 0.021 (See *Spectral Correction* in Table A6.) Given that our integration radius is larger then RCW38's size, the flux contribution of diffuse

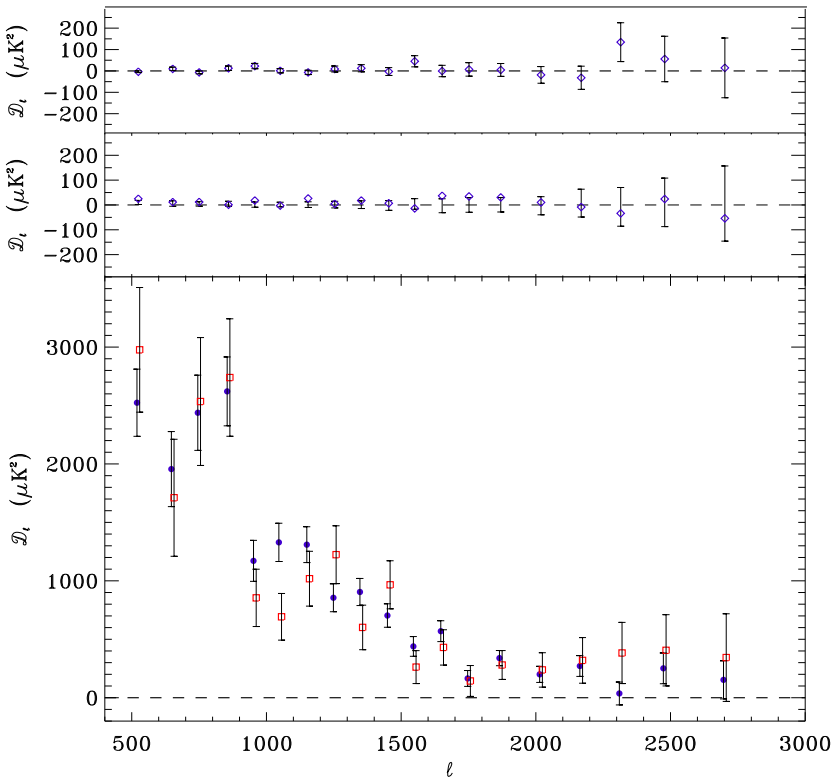

FIG. 2.— Systematic tests performed on the ACBAR data. *Top*: Power spectrum produced from the difference of maps made with left- and right-going chopper sweeps. *Middle*: Power spectrum (diamonds) calculated from the difference of maps made from the first and second halves of the data for each field (CMB2, CMB5, CMB6, and CMB7), compared with Monte Carlo simulations (error bars). *Bottom*: Power spectrum calculated from the LMT sum maps (squares), compared with the joint power spectrum (pre-decorrelated, filled circles). The consistency between two sets of band-powers demonstrates that the residual chopper offsets are below noise. See text for more detail on this test.

emission near RCW38 can be significant. The spectrum of this extended structure may be different from that of RCW38, in which case the calibration ratio would depend on the integration radius. We estimate this uncertainty from the observed variability of the calibration ratio with integration distance.

The calibration value from the real map is normalized by the spectral correction for RCW38 and the signal-only transfer functions estimated for each experiment. The result of this analysis is that the temperature scale for ACBAR's CMB fields in 2002 should be multiplied by 1.128 ± 0.066 relative to the planet-based calibration given in Runyan et al. (2003). Table A6 tabulates the contributing factors and error budget. We now proceed to propagate this RCW38-based calibration to the CMB2 observation done in 2001.

ACBAR 2001-2002 Cross Calibration We carry the 2002 RCW38 calibration into 2001 by comparing the 2001 observations of the CMB2 field to the overlapping 2002 CMB4 field. The fields are reduced to the overlapping region and a power spectrum is calculated for each field. The bands are widened ($\Delta\ell \sim 200$) to avoid large noise correlations between the band-powers. Care was taken to insure the filtering of the two maps only occurs in the overlapped region. However, differences in scan patterns and array configurations between the two seasons cause differences in filtering. We assume that the band-powers from field α and field β are $\mathbf{q}_f$ ($f = \alpha, \beta$). If the relative calibration factor between fields α and β is η, we can find the value η_0 that maximizes the likelihood function:

$$\mathcal{L}(\eta) \propto \exp\left[-\frac{1}{2}\sum_i \frac{(q_{\alpha,i} - \eta q_{\beta,i})^2}{\sigma^2_{D,i}}\right] . \tag{A1}$$

The quantity $\sigma^2_{D,i}$ is the variance of $(q_{\alpha,i} - q_{\beta,i})$ for band i, which can be found by Monte Carlo analysis. A separate Monte Carlo simulation was carried out to confirm that η_0 is an unbiased estimator, and to calculate its uncertainty. We find the calibration factor to be CMB2/CMB4$= 1.238 \pm 0.067$ ($\sqrt{\eta_0}$, in units of temperature). Approximating the uncertainties as Gaussian, it implies the CMB2 temperature scale should be multiplied by 0.911 ± 0.074 relative to the scale used for the analysis of K04.

The day-to-day relative calibration for the 2002 CMB fields is determined using the measured flux of RCW38. The procedures used are outlined in more detail K04. During some parts of 2002, RCW38 observations are only available for one of the two rows of 150 GHz channels. We derive the relative calibration between two rows of bolometers during these periods using the CMB power spectrum comparison method described earlier. We find the corrections to the BOOMERANG-based calibration factors are 1.031 ± 0.025, 0.935 ± 0.050, and 0.998 ± 0.042 for CMB5, CMB6, CMB7,

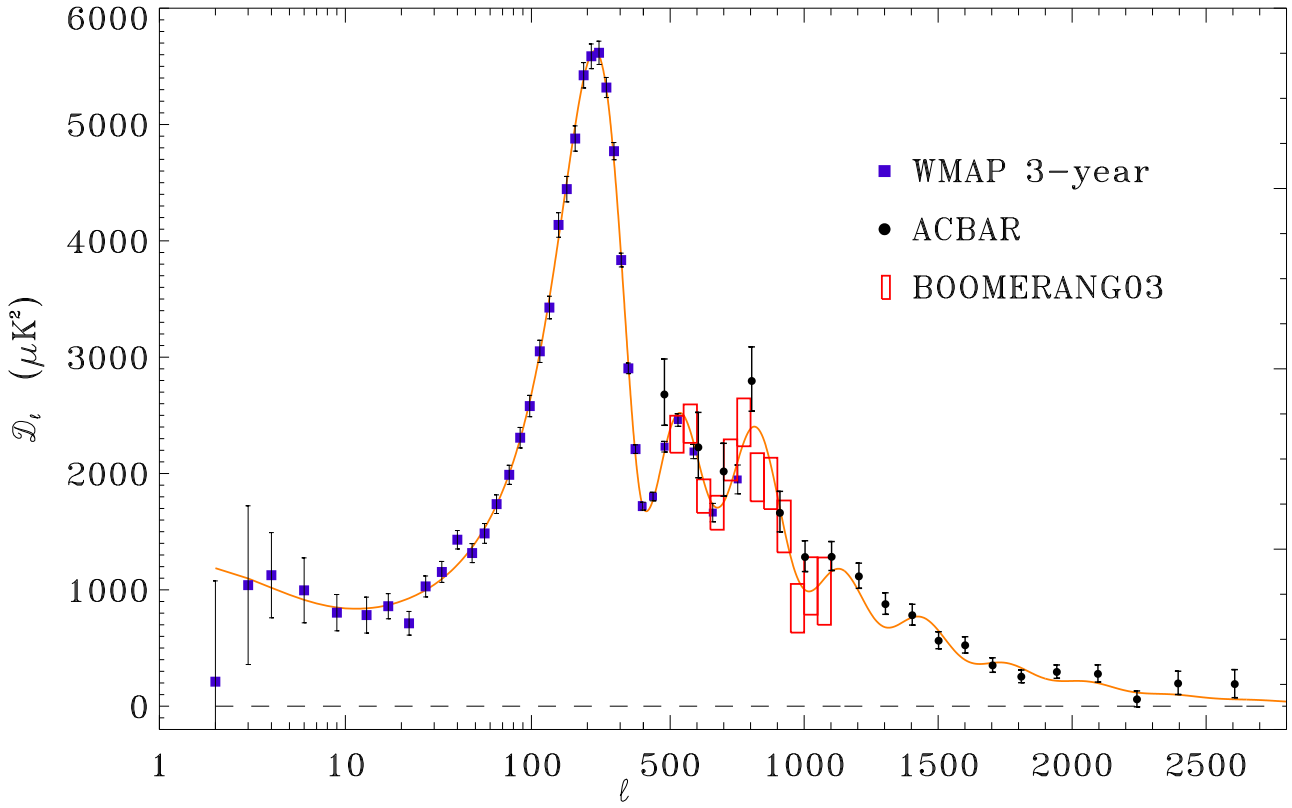

FIG. 3.— The ACBAR band powers plotted with those from WMAP3 (Hinshaw et al. 2006) and the 2003 flight of BOOMERANG (Jones et al. 2006). The three experiments show excellent agreement in the overlapped region.

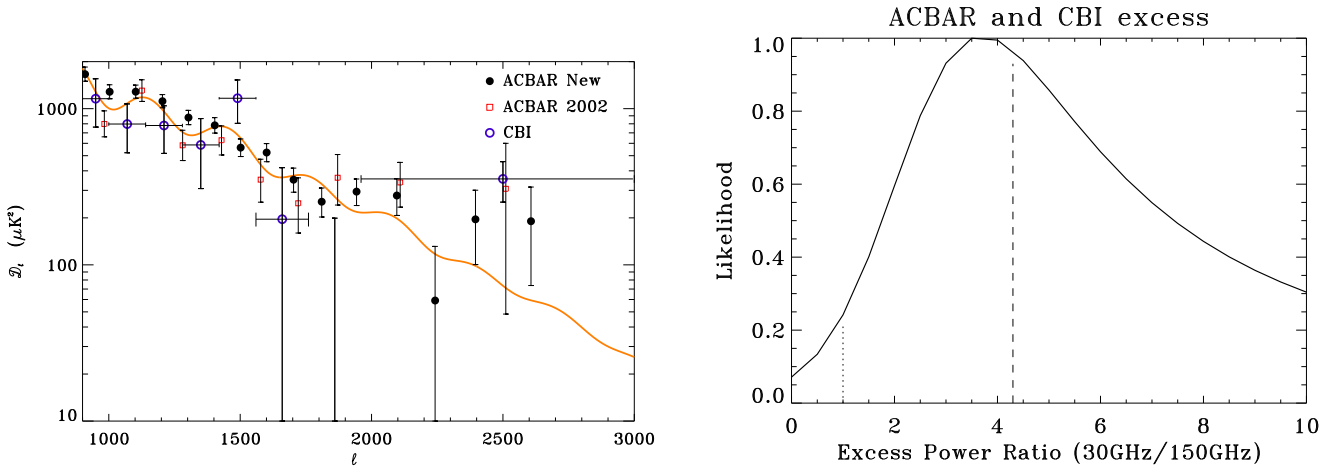

FIG. 4.— ACBAR results on the high-ℓ anisotropies. *Left*: The ACBAR band-powers at $\ell > 1000$, plotted on a logarithmic scale with the latest CBI data taken at a frequency of 30 GHz. All the ACBAR bins at $\ell > 2000$ are lower than the CBI band-power measurement. *Right*: The likelihood distribution for the ratio of the "excess" power, observed by CBI at 30 GHz and ACBAR at 150 GHz. The excess for each experiment is defined as the difference of the measured band-powers and the model band-powers at $\ell > 2000$. The vertical dashed line represents the expected ratio (4.3) for the excess being due to the SZ effect. If the excess power seen in CBI is caused by non-standard primordial processes, the ratio will be unity (blackbody), indicated by the dotted line. We conclude that it is 4.5 times more likely that the excess seen by CBI and ACBAR is caused by the thermal SZ effect than a primordial source. In addition, because of the weak detection of excess power in ACBAR (1.2σ), it is about 3 times more likely that the excess is due to the SZ effect than radio source contamination of the lower frequency CBI data, assuming no contaminations from dusty proto-galaxies.

respectively. We apply these corrections, and determine the overall calibration uncertainty to be 6% (in temperature units) based on the uncertainties associated with B03/ACBAR-2002 RCW38 cross calibration.

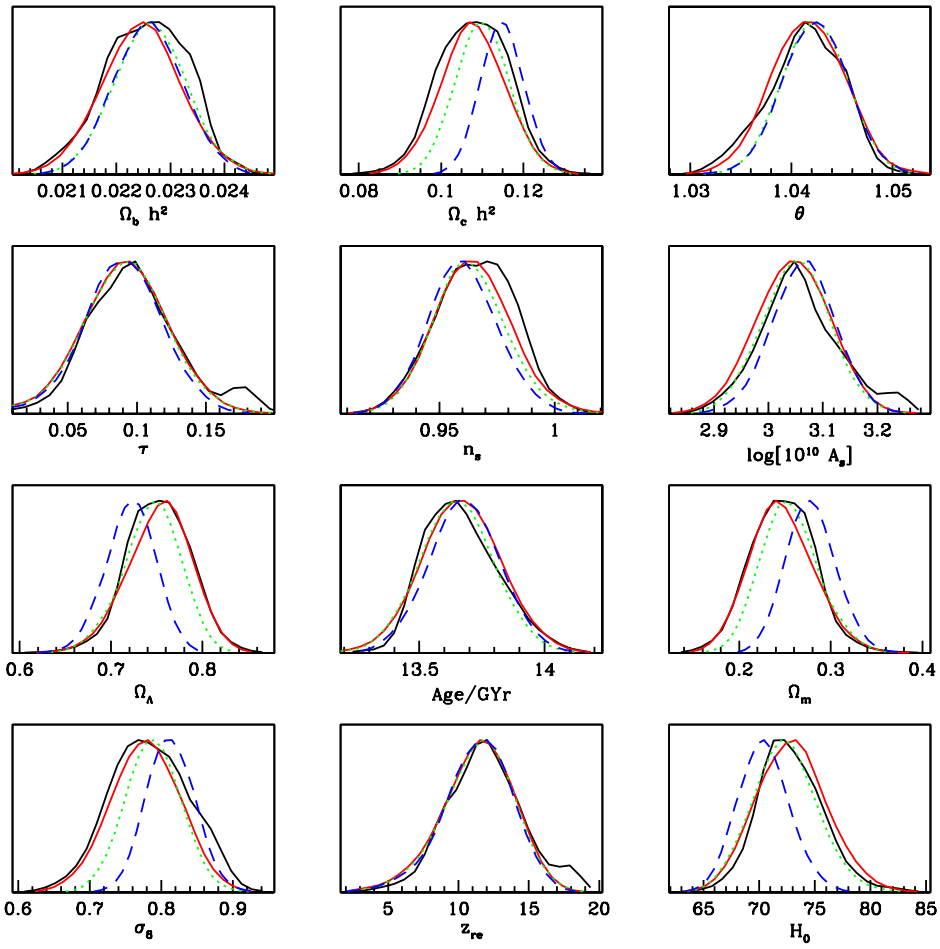

FIG. 5.— Basic parameter marginalized 1-dimensional likelihood distributions for the following data combinations; WMAP3 only (black, solid), ACBAR + WMAP3 (red, dashed), CMBall (green, long-dashed), and CMBall + LSS (blue, dash-dot). All runs include lensing.

REFERENCES

Albrecht, A., Coulson, D., Ferreira, P., & Magueijo, J. 1996, Physical Review Letters, 76, 1413

Bond, J. R., Contaldi, C., & Pogosyan, D. 2003, Royal Society of London Philosophical Transactions Series A, 361, 2435

Bond, J. R., Contaldi, C. R., Pen, U.-L., Pogosyan, D., Prunet, S., Ruetalo, M. I., Wadsley, J. W., Zhang, P.and Mason, B. S., Myers, S. T., Pearson, T. J., Readhead, A. C. S., Sievers, J. L., & Udomprasert, P. S. 2005, ApJ, 626, 12

Bond, J. R., Contaldi, C. R., Pen, U.-L., Pogosyan, D., Prunet, S., Ruetalo, M. I., Wadsley, J. W., Zhang, P., Mason, B. S., Myers, S. T., Pearson, T. J., Readhead, A. C. S., Sievers, J. L., & Udomprasert, P. S. 2005, ApJ, 626, 12

Bond, J. R. & Efstathiou, G. 1984, ApJ, 285, L45

Bond, J. R., Jaffe, A. H., & Knox, L. 1998, Phys. Rev. D, 57, 2117

—. 2000, ApJ, 533, 19, astro-ph/9808264

Borys, C., Chapman, S., Halpern, M., & Scott, D. 2003, MNRAS, 344, 385

Bridle, S. L., Lewis, A. M., Weller, J., & Efstathiou, G. 2003, MNRAS, 342, L72

Burles, S., Nollett, K. M., & Turner, M. S. 2001, ApJ, 552, L1

Bussmann, R. S., Holzapfel, W. L., & Kuo, C. L. 2005, ApJ, 622, 1343

Chapman, S. C., Scott, D., Borys, C., & Fahlman, G. G. 2002, MNRAS, 330, 92

Cole, S., Percival, W. J., Peacock, J. A., Norberg, P., Baugh, C. M., Frenk, C. S., Baldry, I., Bland-Hawthorn, J., Bridges, T., Cannon, R., Colless, M., Collins, C., Couch, W., Cross, N. J. G., Dalton, G., Eke, V. R., De Propris, R., Driver, S. P., Efstathiou, G., Ellis, R. S., Glazebrook, K., Jackson, C., Jenkins, A., Lahav, O., Lewis, I., Lumsden, S., Maddox, S., Madgwick, D., Peterson, B. A., Sutherland, W., & Taylor, K. 2005, MNRAS, 362, 505

Cooray, A., Hu, W., & Tegmark, M. 2000, ApJ, 540, 1

Crill, B. P., Ade, P. A. R., Artusa, D. R., Bhatia, R. S., Bock, J. J., Boscaleri, A., Cardoni, P., Church, S. E., Coble, K., de Bernardis, P., de Troia, G., Farese, P., Ganga, K. M., Giacometti, M., Haynes, C. V., Hivon, E., Hristov, V. V., Iacoangeli, A., Jones, W. C., Lange, A. E., Martinis, L., Masi, S., Mason, P. V., Mauskopf, P. D., Miglio, L., Montroy, T., Netterfield, C. B., Paine, C. G., Pascale, E., Piacentini, F., Polenta, G., Pongetti, F., Romeo, G., Ruhl, J. E., Scaramuzzi, F., Sforna, D., & Turner, A. D. 2003, ApJS, 148, 527

Dawson, K. S., Holzapfel, W. L., Carlstrom, J. E., Joy, M., & LaRoque, S. J. 2006, ApJ, 647, 13

Dickinson, C., Battye, R. A., Carreira, P., Cleary, K., Davies, R. D., Davis, R. J., Genova-Santos, R., Grainge, K., Gutiérrez, C. M., Hafez, Y. A., Hobson, M. P., Jones, M. E., Kneissl, R., Lancaster, K., Lasenby, A., Leahy, J. P., Maisinger, K., Ödman, C., Pooley, G., Rajguru, N., Rebolo, R., Rubiño-Martin, J. A., Saunders, R. D. E., Savage, R. S., Scaife, A., Scott, P. F., Slosar, A., Sosa Molina, P., Taylor, A. C., Titterington, D., Waldram, E., Watson, R. A., & Wilkinson, A. 2004, MNRAS, 353, 732

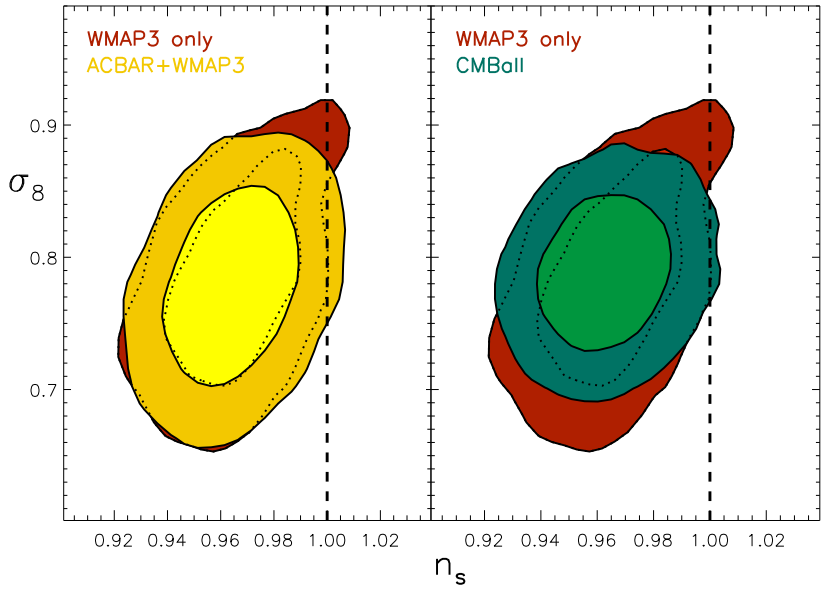

FIG. 6.— Two-dimensional marginalized distribution for the σ_8 and the spectral index n_s. The contours are for the 68% and 95% confidence levels. The underlying (red) region corresponds to the WMAP3 only basic parameter set in both left and right panels. In the left panel the overplotted (yellow) region is for the combination of ACBAR + WMAP3. In the right panel we show the combination ACBAR + CMBall. The Harrison-Zel'dovich-Peebles, scale invariant solution with $n_s = 1$ is only ruled out at the 2σ level.

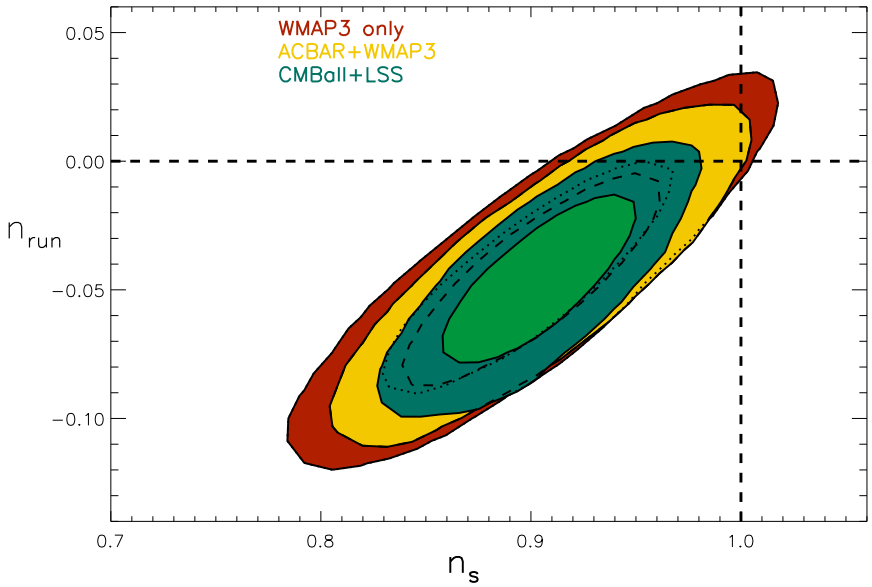

FIG. 7.— Two-dimensional marginalized distribution for the correlated pair $n_{run} = dn_s/d\ln k$ and n_s for the three data combinations. As in Fig. 6, the contours are for the 68% and 95% confidence levels. The straight dashed lines show the scale invariant case. This illustrates that negative running is preferred at less than a 2-σ level. If a tensor component was added, the errors on running would become even larger.

Efstathiou, G., Moody, S., Peacock, J. A., Percival, W. J., Baugh, C., Bland-Hawthorn, J., Bridges, T., Cannon, R., Cole, S., Colless, M., Collins, C., Couch, W., Dalton, G., de Propris, R., Driver, S. P., Ellis, R. S., Frenk, C. S., Glazebrook, K., Jackson, C., Lahav, O., Lewis, I., Lumsden, S., Maddox, S., Norberg, P., Peterson, B. A., Sutherland, W., & Taylor, K. 2002, MNRAS, 330, L29
Finkbeiner, D. P., Davis, M., & Schlegel, D. J. 1999, ApJ, 524, 867
Goldstein, J. H., Ade, P. A. R., Bock, J. J., Bond, J. R., Cantalupo, C., Contaldi, C. R., Daub, M. D., Holzapfel, W. L., Kuo, C., Lange, A. E., Lueker, M., Newcomb, M., Peterson, J. B., Pogosyan, D., Ruhl, J. E., Runyan, M. C., & Torbet, E. 2003, ApJ, 599, 773
Greve, T. R., Ivison, R. J., Bertoldi, F., Stevens, J. A., Dunlop, J. S., Lutz, D., & Carilli, C. L. 2004, MNRAS, 354, 779
Griffiths, L. M., Kunz, M., & Silk, J. 2003, MNRAS, 339, 680
Halverson, N. W., Leitch, E. M., Pryke, C., Kovac, J., Carlstrom, J. E., Holzapfel, W. L., Dragovan, M., Cartwright, J. K., Mason, B. S., Padin, S., Pearson, T. J., Readhead, A. C. S., & Shepherd, M. C. 2002, ApJ, 568, 38
Hanany, S., Ade, P., Balbi, A., Bock, J., Borrill, J., Boscaleri, A., de Bernardis, P., Ferreira, P. G., Hristov, V. V., Jaffe, A. H., Lange, A. E., Lee, A. T., Mauskopf, P. D., Netterfield, C. B., Oh, S., Pascale, E., Rabii, B., Richards, P. L., Smoot, G. F., Stompor, R., Winant, C. D., & Wu, J. H. P. 2000, ApJ, 545, L5
Hinshaw, G., Spergel, D. N., Verde, L., Hill, R. S., Meyer, S. S., Barnes, C., Bennett, C. L., Halpern, M., Jarosik, N., Kogut, A., Komatsu, E., Limon, M., Page, L., Tucker, G. S., Weiland, J. L., Wollack, E., & Wright, E. L. 2006, /apj, submitted, "astro-ph/0603451"
Hu, W. & White, M. 1997, ApJ, 479, 568

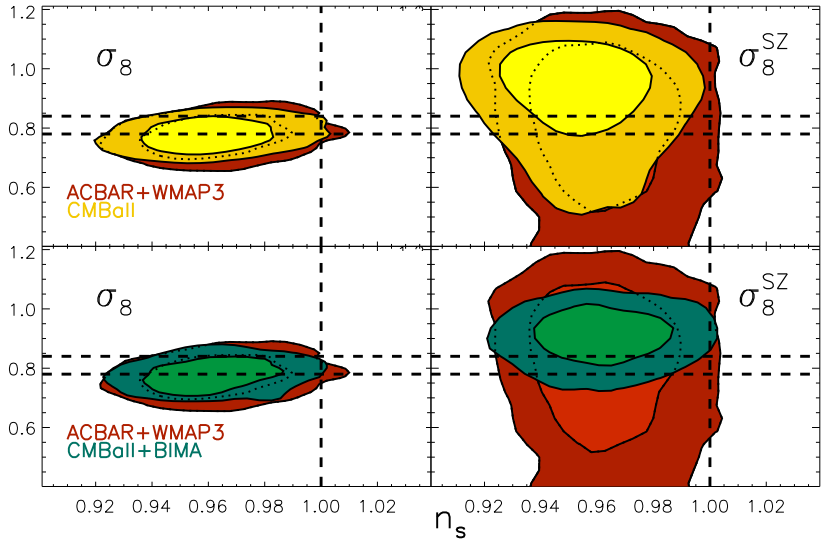

FIG. 8.— Two-dimensional marginalized distribution for the conventional σ_8 parameter (left panels) and SZ template fit derived σ_8^{SZ} (right panel), plotted *vs.* the spectral index n_s. The contours shown are for the 68% and 95% confidence levels. The data combinations used are shown in the insets. The horizontal lines show the 1σ confidence region for the σ_8 parameter obtained from the 1-d marginalized posterior for the CMBall + BIMA + LSS combination with no SZ template fitting. The SZ derived values for the normalization of the matter fluctuations are higher than those found from the basic parameter run.

Huffenberger, K. M., Eriksen, H. K., & Hansen, F. K. 2006, ArXiv Astrophysics e-prints
Jones, W. C., Ade, P. A. R., Bock, J. J., Bond, J. R., Borrill, J., Boscaleri, A., Cabella, P., Contaldi, C. R., Crill, B. P., de Bernardis, P., De Gasperis, G., de Oliveira-Costa, A., De Troia, G., di Stefano, G., Hivon, E., Jaffe, A. H., Kisner, T. S., Lange, A. E., MacTavish, C. J., Masi, S., Mauskopf, P. D., Melchiorri, A., Montroy, T. E., Natoli, P., Netterfield, C. B., Pascale, E., Piacentini, F., Pogosyan, D., Polenta, G., Prunet, S., Ricciardi, S., Romeo, G., Ruhl, J. E., Santini, P., Tegmark, M., Veneziani, M., & Vittorio, N. 2006, ApJ, 647, 823
Knox, L. 1999, Phys. Rev. D, 60, 103516, astro-ph/9902046
Komatsu, E. & Seljak, U. 2002, MNRAS, 336, 1256
Kuo, C. L., Ade, P. A. R., Bock, J. J., Cantalupo, C., Daub, M. D., Goldstein, J., Holzapfel, W. L., Lange, A. E., Lueker, M., Newcomb, M., Peterson, J. B., Ruhl, J. E., Runyan, M. C., & Torbet, E. 2004, ApJ, 600, 32
Laurent, G. T., Aguirre, J. E., Glenn, J., Ade, P. A. R., Bock, J. J., Edgington, S. F., Goldin, A., Golwala, S. R., Haig, D., Lange, A. E., Maloney, P. R., Mauskopf, P. D., Nguyen, H., Rossinot, P., Sayers, J., & Stover, P. 2005, ApJ, 623, 742
Leach, S. M. & Liddle, A. R. 2003, MNRAS, 341, 1151

TABLE A6
ERROR BUDGET FOR THE RCW38 BASED ACBAR CALIBRATION

Source	Value	Uncertainty (%)
Ratio of B03 over ACBAR	1.060	-
Statistical error		0.53
Residual chopper synchronous offsets		0.1
B03 Instrumental noise		0.3
Variability during 2002		2.0
Transfer function:	1.056	-
Statistical error		0.17
Uncertainty in the signal model		3.0
Dependence upon the radius of integration		1.5
Beam uncertainty		1.35
Spectral Correction	1.008	-
RCW38's spectrum and experimental bandpasses		2.1
Spectrum of extended structure		3.0
B03's Absolute Calibration through WMAP		1.8
Overall	1.128	5.84%

NOTE. — The calibration of ACBAR through RCW38 has multiple factors and potential sources of error, tabulated here for reference. The dominant calibration uncertainties are due to uncertainties in the emission spectrum of RCW38 and the morphology and spectrum of the extended galactic structure.

Leitch, E. M., Kovac, J. M., Halverson, N. W., Carlstrom, J. E., Pryke, C., & Smith, M. W. E. 2005, ApJ, 624, 10
Lewis, A. & Bridle, S. 2002, Phys. Rev. D, 66, 103511
Lewis, A., Challinor, A., & Lasenby, A. 2000, ApJ, 538, 473
MacTavish, C. J., Ade, P. A. R., Bock, J. J., Bond, J. R., Borrill, J., Boscaleri, A., Cabella, P., Contaldi, C. R., Crill, B. P., de Bernardis, P., De Gasperis, G., de Oliveira-Costa, A., De Troia, G., di Stefano, G., Hivon, E., Jaffe, A. H., Jones, W. C., Kisner, T. S., Lange, A. E., Lewis, A. M., Masi, S., Mauskopf, P. D., Melchiorri, A., Montroy, T. E., Natoli, P., Netterfield, C. B., Pascale, E., Piacentini, F., Pogosyan, D., Polenta, G., Prunet, S., Ricciardi, S., Romeo, G., Ruhl, J. E., Santini, P., Tegmark, M., Veneziani, M., & Vittorio, N. 2006, ApJ, 647, 799
Maloney, P. R., Glenn, J., Aguirre, J. E., Golwala, S. R., Laurent, G. T., Ade, P. A. R., Bock, J. J., Edgington, S. F., Goldin, A., Haig, D., Lange, A. E., Mauskopf, P. D., Nguyen, H., Rossinot, P., Sayers, J., & Stover, P. 2005, ApJ, 635, 1044
Masi, S., Ade, P., Bock, J., Bond, J., Borrill, J., Boscaleri, A., Cabella, P., Contaldi, C., Crill, B., de Bernardis, P., De Gasperis, G., de Oliveira-Costa, A., De Troia, G., Di Stefano, G., Hivon, E., Jaffe, A., Jones, W. C., Kisner, T., Lange, A., MacTavish, C., Mauskopf, P., Melchiorri, A., Montroy, T., Natoli, P., Netterfield, B., Pascale, E., Piacentini, F., Pogosyan, D., Polenta, G., Prunet, S., Ricciardi, S., Romeo, G., Ruhl, J., Santini, P., Tegmark, M., Veneziani, M., & Vittorio, N. 2006, A&A, 458, 687
Mason, B., Weintraub, L., Pearson, T., Sievers, J., Shepherd, M., & Readhead, A. 2005, in Bulletin of the American Astronomical Society, 1429–+
Mason, B. S., Pearson, T. J., Readhead, A. C. S., Shepherd, M. C., Sievers, J., Udomprasert, P. S., Cartwright, J. K., Farmer, A. J., Padin, S., Myers, S. T., Bond, J. R., Contaldi, C. R., Pen, U., Prunet, S., Pogosyan, D., Carlstrom, J. E., Kovac, J., Leitch, E. M., Pryke, C., Halverson, N. W., Holzapfel, W. L., Altamirano, P., Bronfman, L., Casassus, S., May, J., & Joy, M. 2003, ApJ, 591, 540
Montroy, T. E., Ade, P. A. R., Bock, J. J., Bond, J. R., Borrill, J., Boscaleri, A., Cabella, P., Contaldi, C. R., Crill, B. P., de Bernardis, P., De Gasperis, G., de Oliveira-Costa, A., De Troia, G., di Stefano, G., Hivon, E., Jaffe, A. H., Jones, W. C., Kisner, T. S., Lange, A. E., MacTavish, C. J., Masi, S., Mauskopf, P. D., Melchiorri, A., Natoli, P., Netterfield, C. B., Pascale, E., Piacentini, F., Pogosyan, D., Polenta, G., Prunet, S., Ricciardi, S., Romeo, G., Ruhl, J. E., Santini, P., Tegmark, M., Veneziani, M., & Vittorio, N. 2006, ApJ, 647, 813
Mukherjee, P. & Wang, Y. 2003, ApJ, 599, 1
Peacock, J. A. 1999, Cosmological physics (Cosmological physics. Publisher: Cambridge, UK: Cambridge University Press, 1999. ISBN: 0521422701)
Pearson, T. J., Mason, B. S., Readhead, A. C. S., Shepherd, M. C., Sievers, J. L., Udomprasert, P. S., Cartwright, J. K., Farmer, A. J., Padin, S., Myers, S. T., Bond, J. R., Contaldi, C. R., Pen, U.-L., Prunet, S., Pogosyan, D., Carlstrom, J. E., Kovac, J., Leitch, E. M., Pryke, C., Halverson, N. W., Holzapfel, W. L., Altamirano, P., Bronfman, L., Casassus, S., May, J., & Joy, M. 2003, ApJ, 591, 556
Peiris, H. V., Komatsu, E., Verde, L., Spergel, D. N., Bennett, C. L., Halpern, M., Hinshaw, G., Jarosik, N., Kogut, A., Limon, M., Meyer, S. S., Page, L., Tucker, G. S., Wollack, E., & Wright, E. L. 2003, ApJS, 148, 213
Piacentini, F., Ade, P. A. R., Bock, J. J., Bond, J. R., Borrill, J., Boscaleri, A., Cabella, P., Contaldi, C. R., Crill, B. P., de Bernardis, P., De Gasperis, G., de Oliveira-Costa, A., De Troia, G., di Stefano, G., Hivon, E., Jaffe, A. H., Kisner, T. S., Jones, W. C., Lange, A. E., Masi, S., Mauskopf, P. D., MacTavish, C. J., Melchiorri, A., Montroy, T. E., Natoli, P., Netterfield, C. B., Pascale, E., Pogosyan, D., Polenta, G., Prunet, S., Ricciardi, S., Romeo, G., Ruhl, J. E., Santini, P., Tegmark, M., Veneziani, M., & Vittorio, N. 2006, ApJ, 647, 833
Readhead, A. C. S., Mason, B. S., Contaldi, C. R., Pearson, T. J., Bond, J. R., Myers, S. T., Padin, S., Sievers, J. L., Cartwright, J. K., Shepherd, M. C., Pogosyan, D., Prunet, S., Altamirano, P., Bustos, R., Bronfman, L., Casassus, S., Holzapfel, W. L., May, J., Pen, U.-L., Torres, S., & Udomprasert, P. S. 2004a, ApJ, 609, 498
Readhead, A. C. S., Myers, S. T., Pearson, T. J., Sievers, J. L., Mason, B. S., Contaldi, C. R., Bond, J. R., Bustos, R., Altamirano, P., Achermann, C., Bronfman, L., Carlstrom, J. E., Cartwright, J. K., Casassus, S., Dickinson, C., Holzapfel, W. L., Kovac, J. M., Leitch, E. M., May, J., Padin, S., Pogosyan, D., Pospieszalski, M., Pryke, C., Reeves, R., Shepherd, M. C., & Torres, S. 2004b, Science, 306, 836
Riess, A. G., Strolger, L., Tonry, J., Casertano, S., Ferguson, H. C., Mobasher, B., Challis, P., Filippenko, A. V., Jha, S., Li, W., Chornock, R., Kirshner, R. P., Leibundgut, B., Dickinson, M., Livio, M., Giavalisco, M., Steidel, C. C., Benítez, T., & Tsvetanov, Z. 2004, ApJ, 607, 665
Runyan, M. C. 2002, PhD thesis, California Institute of Technology

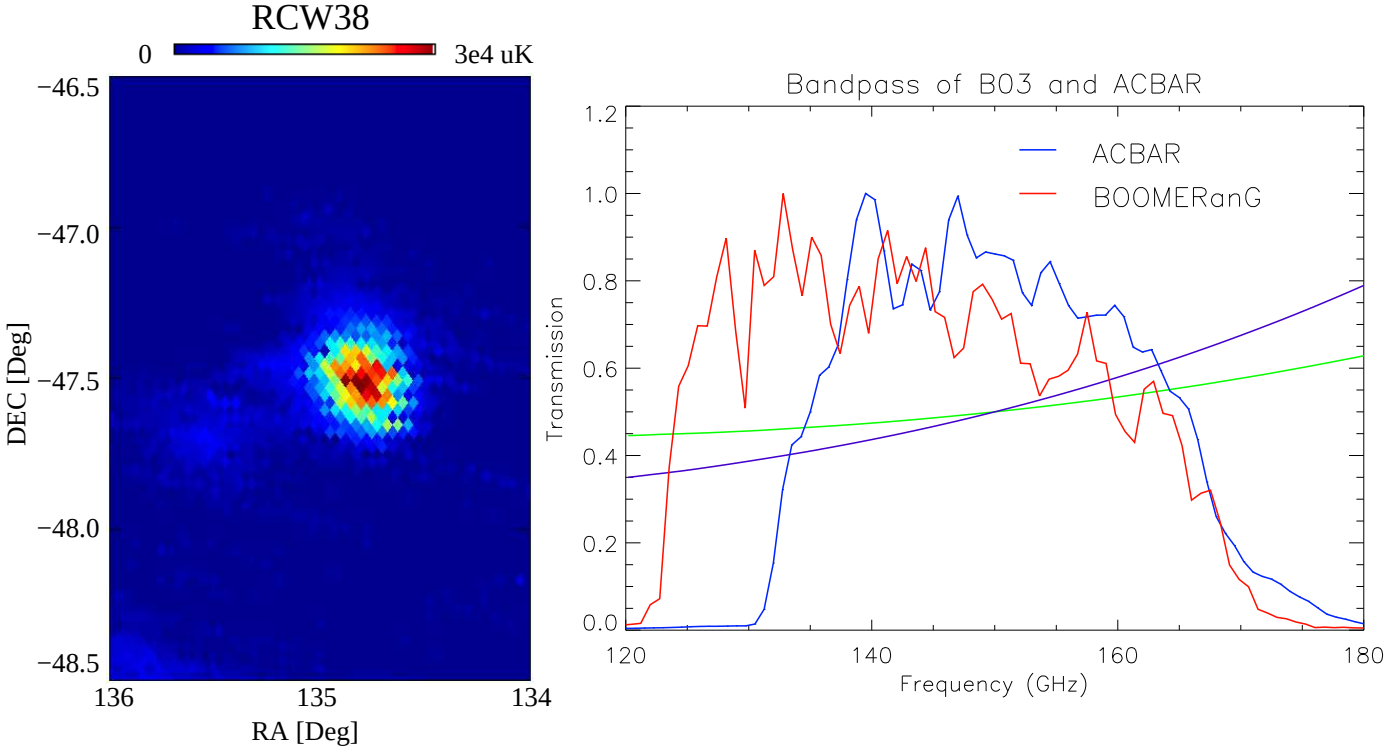

FIG. A9.— On the **left-hand side** is a map of RCW38 made by B03. The bandpasses for each experiment measured by Fourier transform spectroscopy are shown on the **right**. The range of possible spectra (1σ) for RCW38 is also shown, with each spectrum being normalized to 0.50 at 150 GHz. (green and violet lines).

Runyan, M. C., Ade, P. A. R., Bhatia, R. S., Bock, J. J., Daub, M. D., Goldstein, J. H., Haynes, C. V., Holzapfel, W. L., Kuo, C. L., Lange, A. E., Leong, J., Lueker, M., Newcomb, M., Peterson, J. B., Reichardt, C., Ruhl, J., Sirbi, G., Torbet, E., Tucker, C., Turner, A. D., & Woolsey, D. 2003, ApJS, 149, 265
Scott, D. & White, M. 1999, A&A, 346, 1
Seljak, U. 1996, ApJ, 463, 1
Sievers, J. L., Achermann, C., Bond, J. R., Bronfman, L., Bustos, R., Contaldi, C. R., Dickinson, C., Ferreira, P. G., Jones, M. E., Lewis, A. M., Mason, B. S., May, J., Myers, S. T., Padin, S., Pearson, T. J., Pospieszalski, M., Readhead, A. C. S., Reeves, R., Taylor, A. C., & Torres, S. 2005, ArXiv Astrophysics e-prints
Silk, J. 1968, ApJ, 151, 459
Smail, I., Ivison, R. J., Blain, A. W., & Kneib, J.-P. 2002, MNRAS, 331, 495
Spergel, D. N., Bean, R., Dore, O., Nolta, M. R., Bennett, C. L., Hinshaw, G., Jarosik, N., Komatsu, E., Page, L., Peiris, H. V., Verde, L., Barnes, C., Halpern, M., Hill, R. S., Kogut, A., Limon, M., Meyer, S. S., Odegard, N., Tucker, G. S., Weiland, J. L., Wollack, E., & Wright, E. L. 2006, ArXiv Astrophysics e-prints
Spergel, D. N., Verde, L., Peiris, H. V., Komatsu, E., Nolta, M. R., Bennett, C. L., Halpern, M., Hinshaw, G., Jarosik, N., Kogut, A., Limon, M., Meyer, S. S., Page, L., Tucker, G. S., Weiland, J. L., Wollack, E., & Wright, E. L. 2003, ApJS, 148, 175
Subramanian, K., Seshadri, T. R., & Barrow, J. D. 2003, MNRAS, 344, L31
Tegmark, M. 1997, Phys. Rev. D, 55, 5895
Tegmark, M., Strauss, M. A., Blanton, M. R., Abazajian, K., Dodelson, S., Sandvik, H., Wang, X., Weinberg, D. H., Zehavi, I., Bahcall, N. A., Hoyle, F., Schlegel, D., Scoccimarro, R., Vogeley, M. S., Berlind, A., Budavari, T., Connolly, A., Eisenstein, D. J., Finkbeiner, D., Frieman, J. A., Gunn, J. E., Hui, L., Jain, B., Johnston, D., Kent, S., Lin, H., Nakajima, R., Nichol, R. C., Ostriker, J. P., Pope, A., Scranton, R., Seljak, U., Sheth, R. K., Stebbins, A., Szalay, A. S., Szapudi, I., Xu, Y., Annis, J., Brinkmann, J., Burles, S., Castander, F. J., Csabai, I., Loveday, J., Doi, M., Fukugita, M., Gillespie, B., Hennessy, G., Hogg, D. W., Ivezić, Ž., Knapp, G. R., Lamb, D. Q., Lee, B. C., Lupton, R. H., McKay, T. A., Kunszt, P., Munn, J. A., O'Connell, L., Peoples, J., Pier, J. R., Richmond, M., Rockosi, C., Schneider, D. P., Stoughton, C., Tucker, D. L., vanden Berk, D. E., Yanny, B., & York, D. G. 2004, Phys. Rev. D, 69, 103501
Wright, A. E., Griffith, M. R., Burke, B. F., & Ekers, R. D. 1994, ApJS, 91, 111